2020

Electromagnetic modeling of vegetation canopy for retrieving soil moisture and vegetation optical depth

Jeil Park
Iowa State University

Electromagnetic modeling of vegetation canopy for retrieving soil moisture and vegetation optical depth

by

Jeil Park

A thesis submitted to the graduate faculty

in partial fulfillment of the requirements for the degree of

MASTER OF SCIENCE

Major: Electrical Engineering (Electromagnetics Microwave and Nondestructive Evaluation)

Program of Study Committee:
Jiming Song, Major Professor
Brian K Hornbuckle
Meng Lu

The student author, whose presentation of the scholarship herein was approved by the program of study committee, is solely responsible for the content of this thesis. The Graduate College will ensure this thesis is globally accessible and will not permit alterations after a degree is conferred.

Iowa State University

Ames, Iowa

2020

DEDICATION

I would like to dedicate this thesis to my wife Jihye Lee without whose support I would not have been able to complete this work.

TABLE OF CONTENTS

Page

LIST OF TABLES

LIST OF FIGURES

ACKNOWLEDGMENTS

I would like to take this opportunity to express my thanks to those who helped me with various aspects of conducting research and the writing of this thesis. First and foremost, Dr. Jiming Song for his guidance, patience and support throughout this research and the writing of this thesis. His insights and words of encouragement have often inspired me and renewed my hopes for completing my graduate education. I would also like to thank my committee members for their efforts and contributions to this work: Dr. Biran K Hornbuckle and Dr. Meng Lu. I would additionally like to thank Praveen Gurrala, Andrew Downs, Yang Bao, and Myung-Gi Ji for their advice throughout the stages of my graduate career. Finally, I sincerely thank my country for giving me a chance to study abroad, and my family, relatives, and middle school friends for their loving guidance and financial assistance during the writing of this work.

ABSTRACT

The Soil Moisture Active Passive (SMAP) satellite has provided soil moisture estimates in the top 5 cm of the soil surface by measuring the brightness temperature at L-band (f=1.41 GHz, λ=21 cm) emitted from the earth at a spatial resolution of 33 km. The SMAP products have been assessed by comparing them with ground-based in *situ* soil moisture observations. It was found that cropland such as the South Fork located in Iowa is problematic, not satisfying the SMAP accuracy goal. This is due to the vegetation scattering effect which the SMAP algorithm ($\tau - \omega$ model) inherently ignores. Thus, we hypothesize that vegetation scattering effect can not be negligible because of the electrical size of plants comparable to the observation wavelength.

In order to address our hypothesis, we model the vegetation canopy consisting of an infinite number of finite-length cylinders using the Floquet port and periodic boundary condition in the HFSS (high-frequency structure simulator). S-parameters are utilized to derive the reflection and transmission coefficients. The accuracy of this method is validated by comparing it with analytical solutions and the literature.

Three cases are studied: (a) reflection and transmission coefficients for the 2-layer (soil and air) case, (b) vegetation scattering effect for 3-layer (soil, vegetation canopy, and air) case, and (c) transmissivity for the vegetation canopy itself. The results of case (c) show that vegetation optical depth from our HFSS model is about 6.9 times lower than that from the VRT (vector radiative transfer model). Also, the result of the periodically distributed case from our HFSS model falls within the range of results of the sparsely distributed case from the NMM3D (Numerical Maxwell Model in 3D simulations). It is because our HFSS model and the NMM3D take into account the scattered fields and coherent wave interactions by solving Maxwell equation directly. Through these cases, we show that the vegetation scattering effect becomes larger as plants grow taller, and the proposed approach can provide the vegetation optical depth for grass canopy.

CHAPTER 1. OVERVIEW

This chapter includes a short introduction to NASA's Soil Moisture Active Passive (SMAP) mission. SMAP's performance and measurement accuracy limitation in the context of the U.S. Corn Belt are discussed. Electromagnetic modeling of vegetation canopy as part of efforts to reduce SMAP product's seasonal bias in the cropland is introduced. Finally, the thesis format is included.

1.1 Introduction to SMAP

The SMAP mission is an earth observation satellite that estimates the amount of water in the soil surface as a response to the National Research Council's (NRC) decadal survey report released in 2007. The advantage of knowing soil moisture is that it can help improve flood and drought monitoring, weather and climate forecasts, and agricultural productivity. The SMAP was launched in January 2015, but only a radiometer has performed as intended due to the radar becoming unavailable in April 2015 because of irrecoverable damage [6].

As shown in Figure 1.1, an antenna subsystem consisting of a feed horn antenna and a reflector antenna is mounted on the SMAP. It provides a conical scanning beam in order to have a wide swath up to 1,000 km at a constant surface incidence angle near 40°. This novel technique makes it possible for the SMAP to have a near-global coverage and 3-day revisit time due to its wide swath. The radiometer electronic subsystem measures the polarized brightness temperature at L-band (f=1.41 GHz, λ=21 cm) emitted from the earth at a spatial resolution of 33 km. By incorporating the brightness temperature and ancillary data sets into SMAP's retrieval algorithm, the SMAP finally estimates soil moisture [3].

In 2018, the SMAP performance assessment was conducted as compared with the ground-based in *situ* soil moisture observations between April 2015 and October 2016. It was found that the

SMAP offered high-quality soil moisture estimates over the period above, and a SCA-V (single channel algorithm using T_{Bv}) implemented in the SMAP provided the overall best performance for most CVSs (core validation sites) [11]. However, it did not produce the reliable soil moisture estimates for the cropland validation site, such as the South Fork located in Iowa, showing the ubRMSE (unbiased root-mean-square error) 0.054 $m^3 \cdot m^{-3}$ greater than 0.04 $m^3 \cdot m^{-3}$ of the SMAP accuracy goal.

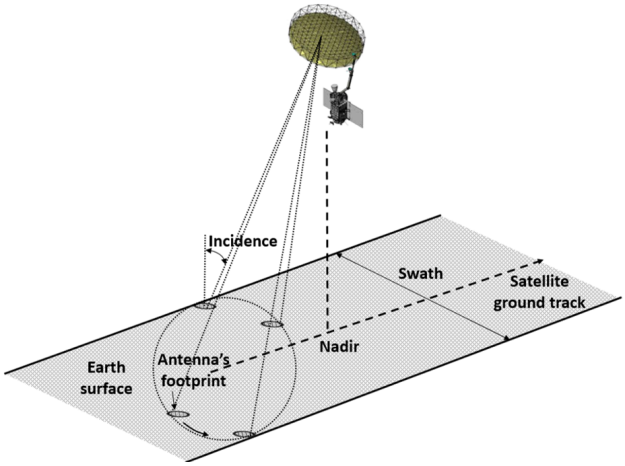

Figure 1.1 Configuration of SMAP observation showing the conical scanning beam and antenna's footprint [3].

1.2 Research Motivation and Objective

1.2.1 SMAP Performance in the U.S. Corn Belt

In order to improve the SMAP performance in croplands, it is essential to look into soil characteristics of the South Fork core validation site. About 85% of this site is dominated by cropland consisting of corn (67%) and soybean (33%). The soil is classified by loam and silty clay loam and retains water for a large portion of the year, as shown in Figure 1.2 [12].

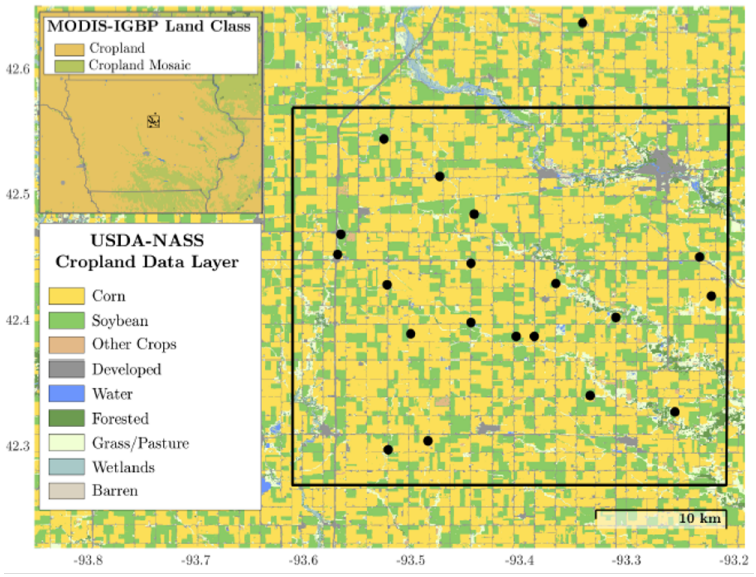

(a)

[Tillage before planting]

[Crop emergence]

[Crop maturity]

[Tillage After harvest]

(b)

Figure 1.2 (a) The South Fork core validation site in the Corn Belt state of Iowa showing in *situ* stations(•) and the 33 km radiometric resolution(□) of the nearest SMAP footprint (b) View of seasonal changes in crop field indicating soil roughness and crop growth [1].

The SMAP performance in the South Fork CVS was validated again in 2019, as shown in Table 1.1, where the dry bias indicates that the SMAP estimates a lesser amount of soil moisture than in *situ* observations, and the ubRMSE describes the accuracy of the SMAP product. The large dry bias occurred in early-spring and late-fall when tillage takes place before planting and after harvest. Also, the relatively small dry bias still presented during July-October when crops start to cover the soil surface and grow up to maturity, as shown in Figure 1.2. In addition to this, the large ubRMSE emerged in May-June when the stem of crops proliferates.

Table 1.1 Bias and ubRMSE between SMAP Level 2 Soil Moisture (L2SM) and South Fork weighted average soil moisture(WASM) [1]

Single Channel Algorithm Applied to v-pol T_B (SCA-V)										
2018 Year	**Mar**	**Apr**	**May**	**Jun**	**Jul**	**Aug**	**Sep**	**Oct**	**Nov**	**All**
Bias, m^3m^{-3}	-0.035	-0.078	-0.020	0.044	-0.029	-0.026	-0.020	-0.021	-0.088	**-0.027**
ubRMSE, m^3m^{-3}	0.060	0.021	0.042	0.051	0.032	0.027	0.035	0.038	0.042	**0.051**

This seasonal bias can be accounted for by soil surface roughness and the vegetation scattering effect. First, even though tillage roughens the soil surface, SMAP's retrieval algorithm assumes that soil surface is not modified over time and hence incorrectly interprets rougher soil surface as an increase in the vegetation optical depth (VOD). Since the VOD is defined as the degree to which microwave radiation is attenuated by vegetation, the increase in the VOD does not physically make sense when plants do not grow in the context of tillage [13]. Second, a zeroth-order radiative transfer model ($\tau-\omega$ model), which SMAP's algorithm uses, inherently treats vegetation scattering as almost zero, which is not consistent with the physical phenomenon that happens on the cropland. When the electrical size of plants becomes comparable to the wavelength (λ=21 cm), some amount of total emission along the way to the SMAP satellite scatters in another direction, which causes the observed brightness temperature to lower (called scatter darkening). Thus, the vegetation scattering can not be negligible, and $\tau-\omega$ model is suggested to be applied to a lower scattering situation [14]. Third, as the crops begin to cover the soil surface with its stem, leaves, and ear

during the growing season, the SMAP satellite rarely sees the soil surface and the sensitivity to soil moisture degrades. Therefore, these causes result in the inaccuracy of the SMAP performance.

1.2.2 Modeling for Vegetation Canopy

It is necessary to explain what precisely the vegetation scattering means before introducing our proposed approach. When an electromagnetic wave excites the molecules in a plant (e.g., corn, grass, and soybean) so that they rotate, vibrate, and collide with each other in a certain way, electric charges are accelerated. Thus, the scattered radiation from plant is generated, some of which travel into the SMAP antenna. Furthermore, since crops are generally planted in periodically-spaced rows, and its stem is of vertical structure, the scattered radiation generated from all of the plants can retain the coherency as well as polarization [15].

Researchers have attempted to make SMAP's algorithm suitable in croplands and have suggested modifying the $\tau - \omega$ model in order to take into account the vegetation scattering properly. This is because the effect of vegetation scattering on the brightness temperature observed by SMAP gets significant as a result of increasing biomass in cropland, or the size of plants being comparably larger than the wavelength [16, 17].

We hypothesize that modeling the vegetation canopy using the HFSS (high-frequency structure simulator) can make it possible for us to show that the vegetation scattering effect can not be negligible as plants grow taller. Also, the vegetation optical depth depending on different types of cropland can be computed in our proposed method where the scattered fields from plants and coherent wave interactions are considered by solving Maxwell equation directly.

In our proposed method, the vegetation canopy consisting of an infinite number of a cylinder that represents plant's stem in cropland is modeled by using the PBC (periodic boundary condition), and a plane wave is generated by the Floquet port [18]. The HFSS solution using the unit cell analysis provides scattering parameters. In this manner, we determine the reflectivity and transmissivity of the vegetation canopy via S-parameters. Therefore, we are able to prove our hypothesis because the transmissivity is directly related to the VOD. We also model plant's stem with different heights and

soil surface together to observe the vegetation scattering effect. In order to validate our proposed approach, the simulation results are compared with analytical solutions and literature.

1.3 Thesis Format

The following Chapter 2 describes how SMAP algorithm estimates the soil moisture along with the explanation of the relationship between the received power by an antenna and brightness temperature, emissivity, the $\tau - \omega$ model, effective temperature, and soil surface roughness. The understanding of the soil moisture retrieval algorithm helps to develop our electromagnetic modeling of vegetation canopy and analyze the simulation results.

Chapter 3 explains how the vegetation canopy and soil are modeled and how the plane wave is generated with the oblique incidence angle. Also, the basic concepts of the Floquet modes and the unit cell analysis are included.

Chapter 4 presents our simulation results for various cases: (a) reflection and transmission coefficients for the 2-layer (soil and air) case, (b) vegetation scattering effect for 3-layer (soil, vegetation canopy, and air) case, and (c) transmissivity for the vegetation canopy itself. The accuracy of our HFSS model is validated by comparing it with an analytical solution and the literature.

Finally, the conclusion is in Chapter 5.

CHAPTER 2. SOIL MOISTURE RETRIEVAL MODEL REVIEW

This chapter illustrates how the radiometer calculates the brightness temperature based on the received power measured by the antenna. Also, the definition of emissivity is introduced. Reviewing the zeroth-order radiative transfer model and the inverse algorithm makes it easier to understand the causes of the problem of the SMAP performance in cropland mentioned in Chapter 1. Additionally, the need to take into account the first-order vegetation scattering is discussed.

2.1 Relations between the Brightness Temperature, Emissivity, and Soil Moisture

A field of spectral brightness generated from the region corresponding to the antenna's footprint is incident upon the SMAP antenna as shown in Figure 2.1. The brightness temperature can be obtained from the resulting power measured by the radiometer, and hence we can derive the emissivity. This section includes formulations from which the relation between the received power and brightness temperature is established [19] and describes the soil moisture corresponding to the brightness temperature.

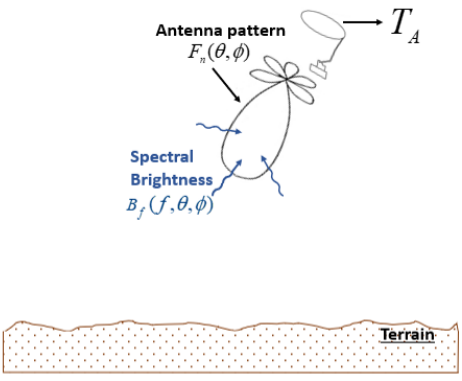

Figure 2.1 A field of spectral brightness B_f incident upon the antenna and antenna temperature T_A.

The received power P_{rec} measured by the antenna can be expressed as

$$P_{\text{rec}} = \frac{1}{2} A_{\text{eff}} \int_{4\pi} \int_{f_0-\Delta f/2}^{f_0+\Delta f/2} B_f(f,\theta,\phi)\, F_n(\theta,\phi)\, d\Omega\, df \tag{2.1}$$

where 1/2 means that only half of the incident radiation can be measured due to all antennas being polarized, A_{eff} is an effective area of antenna aperture (m^2), 4π means that the integration includes all directions, f_0 is a center frequency (Hz), Δf is a bandwidth, $B_f(f,\theta,\phi)$ is spectral brightness ($\text{W m}^{-2}\,\text{sr}^{-1}\,\text{Hz}^{-1}$), and $F_n(\theta,\phi)$ is a normalized antenna pattern acting as a weighting function.

Applying a blackbody cavity assumption and then a Rayleigh-Jeans approximation in the microwave region, $B_f(f,\theta,\phi)$ can be approximated as

$$B_f(f,\theta,\phi) = B_f^b(f,T_A) = \frac{2hf^3}{c^2}\left(\frac{1}{e^{hf/(kT_A)}-1}\right) \approx \frac{2k}{\lambda^2} T_A \tag{2.2}$$

where h is Plank's constant (6.626×10^{-34} J·s), c is speed of light in a vacuum (2.998×10^{8} m·s^{-1}), k is Boltzmann's constant (1.381×10^{-23} J·K^{-1}), λ is a wavelength (m) corresponding to frequency f, T_A is the antenna temperature (K), and also referred to as the temperature of an equivalent blackbody cavity that produces the same power as the actual incident field of spectral brightness.

For the SMAP antenna properties, the bandwidth Δf of about 20 MHz is much less than the center frequency f_0 of 1.41 GHz such that B_f in (2.2) is approximately constant over Δf (i.e., $\Delta f \ll f_0$). Thus, (2.1) simplifies to

$$P_{\text{rec}} = \frac{1}{2} A_{\text{eff}}\, \Delta f\, \frac{2k}{\lambda^2} T_A \int_{4\pi} F_n(\theta,\phi)\, d\Omega \tag{2.3}$$

The integral and A_{eff} in (2.3) are related to the pattern solid angle Ω_P which is defined as

$$\int_{4\pi} F_n(\theta,\phi)\, d\Omega = \Omega_P, \qquad A_{\text{eff}} = \frac{\lambda^2}{\Omega_P} \tag{2.4}$$

Substituting (2.4) into (2.3), P_{rec} is finally simplified to

$$P_{\text{rec}} = k\, T_A\, \Delta f \tag{2.5}$$

It is noted that the power measured by a microwave radiometer is directly proportional to the antenna temperature. The average brightness temperature T_B of the antenna footprint is obtained

by applying correction factors such as radiation efficiency, beam efficiency, and noise temperature of the antenna itself to the antenna temperature T_A.

The microwave emissivity, e, of soil surface is defined as the ratio as brightness temperature T_B of land surface to the physical temperature. This yields,

$$e = \frac{T_B}{T}, \qquad T_B = e\,T \tag{2.6}$$

In the context of the SMAP performance, the physical temperature T is ancillary data and estimated independently. Thus, the emissivity can be determined by measuring the brightness temperature. Also, under conditions of thermodynamic equilibrium of the Kirchhoff's law, the specular emissivity for each polarization is given by

$$e_h^{\text{s,smooth}}(\theta) = \frac{T_{Bh}(\theta)}{T} = 1 - \Gamma_h^{\text{s,smooth}}(\theta) = 1 - \left| \frac{\cos\theta - \sqrt{\epsilon_r - \sin^2\theta}}{\cos\theta + \sqrt{\epsilon_r - \sin^2\theta}} \right|^2 \tag{2.7}$$

$$e_v^{\text{s,smooth}} = \frac{T_{Bv}(\theta)}{T} = 1 - \Gamma_v^{\text{s,smooth}}(\theta) = 1 - \left| \frac{\epsilon_r\cos\theta - \sqrt{\epsilon_r - \sin^2\theta}}{\epsilon_r\cos\theta + \sqrt{\epsilon_r - \sin^2\theta}} \right|^2 \tag{2.8}$$

where a subscript h or v denotes a horizontal or vertical polarization, θ is a viewing or incidence angle of the SMAP antenna, $\Gamma^{\text{s,smooth}}$ is Fresnel power reflectivity of a smooth soil surface, ϵ_r is a dielectric constant of soil, and the term inside an absolute function in (2.7), and (2.8) represents the Fresnel reflection coefficient for each polarization [5].

The basic components of soil are soil particles, water, and air, where the dielectric constant of water is around 80, and dry soil is around $\epsilon_r \sim 5$ at L-band. Thanks to the huge difference between water and dry soil dielectric constants, we can have good sensitivity to soil moisture. For example, as the soil moisture decreases, the soil dielectric constant ϵ_r decreases. This results in a decrease in reflectivity and an increase in soil emissivity. From (2.6), the increase in soil emissivity also leads to an increase in brightness temperature for a given physical soil surface temperature. In short, the decrease in the soil moisture results in an increase in brightness temperature.

In conclusion, these relationships between brightness temperature, emissivity, soil dielectric constant, and soil moisture form the physical basis of the SMAP algorithm.

2.2 Radiative Transfer Modeling of Vegetation

2.2.1 Advantages of L-Band Frequencies

Knowing advantages of 1.4 GHz at L-band provides insight into the radiative transfer model. The advantages are as follows:

- The Rayleigh-Jeans approximation to Plank's law in (2.2) can be used such that we can express the equation of the received power in terms of the brightness temperature.
- A large difference between water dielectric constant $\epsilon_r \sim 80$ and dry soil dielectric constant $\epsilon_r \sim 5$ at the microwave region gives sensitivity to change in the soil moisture.
- The wavelength of L-band frequencies (f=1 to 2 GHz, λ=15 to 30 cm) is typically larger than the soil surface irregularity such that the effect of the roughness of soil surface on the soil moisture sensitivity is small.
- The size of atmospheric particles (range in size from a few nanometers to tens of micrometers in diameter) is considerably smaller than the L-band wavelength. Thus, the atmosphere is almost transparent, and hence, the radiation does not get attenuated when traveling into the atmosphere. The SMAP can provide soil moisture products regardless of weather conditions.
- Transmissivity of vegetation canopy at L-band (1.4 GHz) is higher than at C-band (6 GHz) or X-band (10 GHz), as shown in Figure 2.2, such that soil emission does not vanish after traveling through the vegetation canopy [4].
- The wet soil emitting depth at 1.4 GHz is around 4.8 cm, as shown in Figure 2.2. This indicates that only $1/e$ (about 37 %) of the radiation emitted at around soil depth of 4.8 cm reaches the soil surface and contributes to the observed brightness temperature. Also, using higher frequencies decreases the emitting depth and causes less useful information regarding soil moisture. Thus, using the L-band frequencies make it possible for the SMAP to produce average soil moisture in a few centimeters below the soil surface.

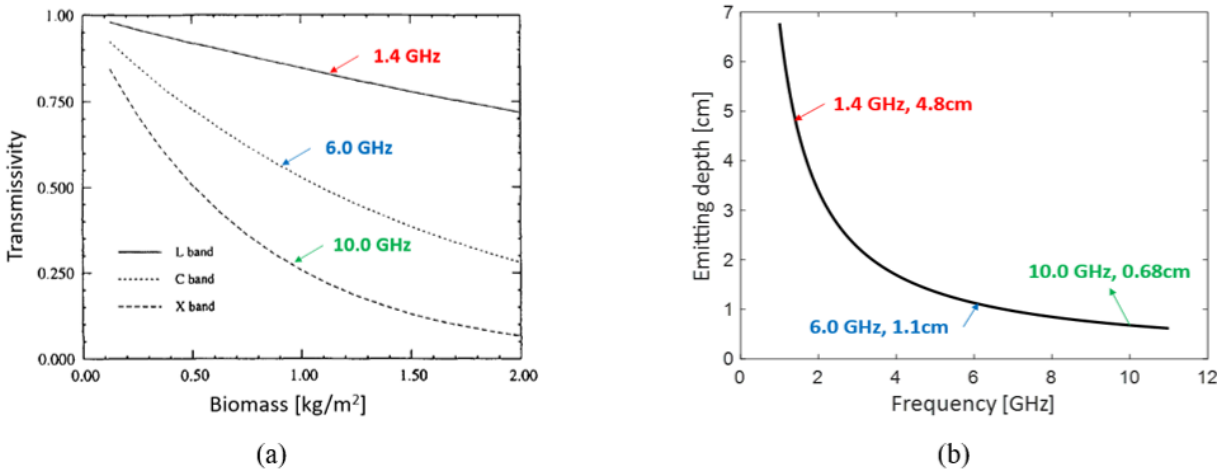

Figure 2.2 (a) Vegetation transmissivity to soil emission over the frequencies (b) Soil emitting depth over the frequencies where wet soil dielectric constant $\epsilon_r = 18 - j3$ [4].

2.2.2 Zeroth-order Radiative Transfer Model

In the presence of vegetation canopy, the soil and vegetation emission have primary contribution to the observed brightness temperature in microwave region. In order to account for the vegetation canopy effects on the antenna footprint, the SMAP uses a zeroth-order radiative transfer model. Since this model consists of vegetation optical depth τ and single-scattering albedo ω, its another name is the $\tau - \omega$ model. In this model, the vegetation canopy is treated as a homogeneous and isothermal layer over the soil surface, and the scattering within the vegetation canopy is almost zero at the L-band. Therefore, in order for (2.9) to make sense physically, ω must be small and less than 0.1 [20], [21].

The equation of the $\tau - \omega$ model is as follows:

$$\begin{aligned} T_{Bp} = {} & T_{\text{eff}} \left(1 - \Gamma_p^{\text{s,rough}}\right) e^{-\tau/\cos\theta} + (1-\omega)\, T_{\text{eff}} \left(1 - e^{-\tau/\cos\theta}\right) \\ & + (1-\omega)\, T_{\text{eff}} \left(1 - e^{-\tau/\cos\theta}\right) \Gamma_p^{\text{s,rough}}\, e^{-\tau/\cos\theta} \end{aligned} \tag{2.9}$$

where T_{Bp} is the brightness temperature measured by the SMAP radiometer, subscript p refers to the vertical or horizontal polarization, T_{eff} is an effective temperature of the soil and vegetation,

which is typically assumed to be the same at the SMAP overpass time of 6 am, $\Gamma_p^{\text{s,rough}}$ is a reflectivity of rough soil surface, and an emissivity of the rough soil surface $e_p^{\text{s,rough}}$ is $1 - \Gamma_p^{\text{s,rough}}$.

In (2.9), the first term represents the upwelling soil emission that gets attenuated by the vegetation canopy, the second term is the upwelling vegetation emission, and the third term is the downwelling vegetation emission that is reflected by the rough soil surface and gets attenuated as it passes through the vegetation canopy. Thus, three kinds of emission have contribution to the observed brightness temperature by the SMAP as shown in Figure 2.3.

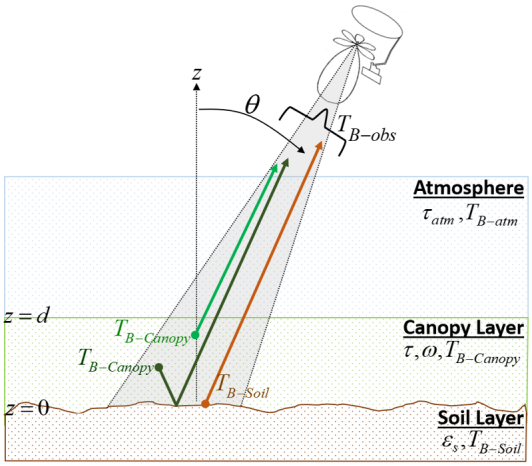

Figure 2.3 Soil and vegetation emission captured by the SMAP antenna [5].

2.2.2.1 Single Scattering Albedo

The single scattering albedo ω is defined as the ratio of the scattering coefficient to the total extinction coefficient; in other words, ω accounts for scattering in the vegetation canopy. For example, when ω=0, then there is no scattering within the vegetation. If we input some value of ω into (2.9), the emission along the way to the SMAP satellite scatters out in another direction, which causes a decrease in the observed brightness temperature (called scatter darkening).

Also, ω depends on the vegetation type, such as the plant's structure and electrical properties. Values of ω are calibrated to best fit the brightness temperature in $\tau - \omega$ model compared with

experimental data [22]. As a result, the single scattering albedo is given in the SMAP ancillary data sets, where all ω values are less than 0.1, as shown in Figure 2.4.

Land Cover Class	h	b	ω
Evergreen needleleaf forest (ENF)	0.160	0.100	0.050
Evergreen broadleaf forest (EBF)	0.160	0.100	0.050
Deciduous needleleaf forest (DNF)	0.160	0.120	0.050
Deciduous broadleaf forest (DBF)	0.160	0.120	0.050
Mixed forest (MXF)	0.160	0.110	0.050
Closed shrublands (CSH)	0.110	0.110	0.050
Open shrublands (OSH)	0.110	0.110	0.050
Woody savannas (WSV)	0.125	0.110	0.050
Savannas (SAV)	0.156	0.110	0.080
Grasslands (GRS)	0.156	0.130	0.050
Croplands (CRP)	0.108	0.110	0.050
Urban and built-up (URB)	0.000	0.100	0.030
Cropland/vegetation Mosaic (MOS)	0.130	0.110	0.065
Barren or sparsely vegetated (BAR)	0.150	0.000	0.000

(a)

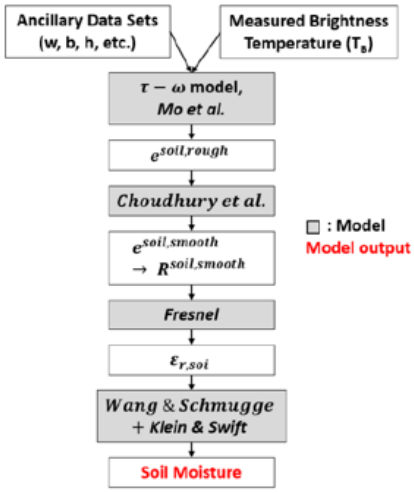

(b)

Figure 2.4 (a) Example of the SMAP ancillary data sets [6] (b) Flowchart illustrating the basic concept of the soil moisture retrieval process [7].

2.2.2.2 Vegetation Optical Depth

The vegetation optical depth τ is a key parameter to represent the attenuation within the vegetation canopy. The radiative transfer model [20] is used to match the observed brightness temperature over the vegetation canopy by adjusting τ. Besides, researcher found that the vegetation optical depth τ is directly proportional to the water column density M_w [23]. This yields

$$\tau = bM_w \tag{2.10}$$

where b is the slope of the regression line and depends on the wavelength (frequency), the vegetation type, and polarization. M_w is defined as the ratio of the mass of water within vegetation tissue to ground area and can be estimated from the Normalized Difference Vegetation Index (NDVI) which is obtained from another satellite. Briefly, during the SMAP performance, M_w is extracted from the another platform (NDVI), and then given the ancillary data b for the vegetation type, the SMAP algorithm calculates the vegetation optical depth τ.

Also, τ can be calculated numerically by

$$\tau = \kappa_e \, d, \qquad \kappa_e = n_0(\sigma_a + \sigma_s) \tag{2.11}$$

where d is the height of vegetation canopy (m), and κ_e is the extinction coefficient ($\mathrm{Np{\cdot}m^{-1}}$) known as a power attenuation coefficient. Under the Foldy's approximation, κ_e depends on three factors; n_0 is the number of identical scatterers per m^3, σ_a is the absorption cross section of a single cylinder, and σ_s is the scattering cross section of a single cylinder [2]

In addition, the transmissivity γ is computed by using (2.12) and defined as the ratio of the transmitted power to incident power. Also, transmissivity depends on the vegetation optical depth τ and the incident angle θ as follows:

$$\gamma = \exp(-\tau \, \sec\theta) \tag{2.12}$$

2.2.2.3 Soil Surface Roughness

A typical soil surface is not a flat smooth surface but has irregularity caused by the soil texture, aggregate size, rock fragment, and human activity such as tillage on the cropland. The effect of soil surface roughness on the brightness temperature measured by the radiometer has been studied by modifying the Fresnel reflectivity [24]. The SMAP uses the following equation:

$$\Gamma^{\mathrm{s,rough}} = \Gamma^{\mathrm{s,smooth}} \exp(-h \cos^2\theta) \tag{2.13}$$

The parameter h is related to the soil surface height variations and depends on the irregularity of soil surface, polarization, and wavelength. It is observed from (2.13) that if the soil roughens, h increases, and then $\Gamma^{\mathrm{s,rough}}$ decreases. As a result, the emissivity increases.

In conclusion, the parameters of ω, b, and h are ancillary datasets and will be provided in the inverse soil moisture algorithm.

2.2.3 Inverse Passive Soil Moisture Algorithm

The overall soil moisture retrieval process shown in Figure 2.4 illustrates how the soil moisture is estimated. The brightness temperature T_B is measured by the SMAP radiometer. Incorporating

the ancillary data sets into $\tau-\omega$ model, the emissivity of the rough soil surface $e_p^{\text{s,rough}}$ is calculated. The formulations below follow [5].

By dividing the T_{eff} on the both sides in (2.9) and substituting (2.6) and (2.12) into (2.9), the total emissivity e_p^{total} is given by

$$e_p^{\text{total}} = (1-\omega)(1-\gamma)[1+(1-e_p^{\text{s,rough}}\,\gamma)] + e_p^{\text{s,rough}}\,\gamma \tag{2.14}$$

and then rearranging (2.14) yields

$$e_p^{\text{s,rough}} = \frac{e_p^{\text{total}} - 1 + \gamma^2 + \omega - \omega\gamma^2}{\gamma^2 + \omega\gamma - \omega\gamma^2} \tag{2.15}$$

where e_p^{total} is the measured value, and γ and ω are the ancillary data sets.

The Fresnel reflectivity $\Gamma_p^{\text{s,smooth}}$ is obtained by using an ancillary data h and the [24] model. This yields

$$e_p^{\text{s,smooth}} = 1 - (1 - e_p^{\text{s,rough}})\,\exp(h\cos^2\theta) \tag{2.16}$$

$$\Gamma_p^{\text{s,smooth}} = 1 - e_p^{\text{s,smooth}} \tag{2.17}$$

Through the Fresnel equation (2.7) and (2.8), the soil dielectric constant ϵ_r is calculated. Finally, the soil moisture is estimated by using the dielectric mixing model [25] with an ancillary data of the soil texture.

2.3 Vegetation Scattering Effect

The primary assumption of the $\tau-\omega$ model is that the effect of vegetation scattering on the brightness temperature is weak at L-band. However, this assumption is not valid at cropland where the size of plants gets significant over the season compared with the wavelength at L-band (f=1.41 GHz, λ=21 cm). Thus, it is essential to take into account the vegetation scattering effect in order to improve the SMAP performance accuracy [14]. In the context of our modeling, we account for the vegetation scattering effect as shown in Figure 2.5. As mentioned in Chapter 1, the scattered fields are generated when the soil thermal radiation is incident upon plants. In addition, the scattered fields have not only the polarization but also the coherency since crops are typically planted in regularly-spaced rows and vertical structures.

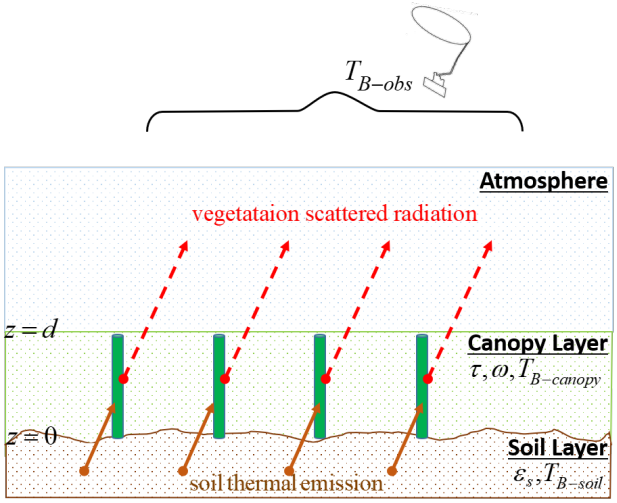

Figure 2.5 Vegetation scattered fields that have contribution to the overall brightness temperature.

CHAPTER 3. MODELING OF SCATTERING PARAMETER BY VEGETATION CANOPY USING HFSS

As mentioned in Chapter 2, we described the causes of SMAP's inaccuracy in croplands and briefly introduced our proposed approach. This chapter includes an explanation of how we model the vegetation canopy in order to account for the vegetation scattering. In addition, the basic concept of Floquet modes and unit cell analysis are included, which can help an interpretation of the S-parameters derived by simulation and develop our model.

3.1 Modeling of Vegetation Canopy

3.1.1 Vegetation Canopy Description in Remote Sensing Point of View

It is essential to mention the definition of coherency and polarization before introducing the vegetation canopy model. Coherency indicates that a phase difference between waves is constant, and hence the sum of these waves exhibits an interference pattern. Also, in the remote sensing area, we assume that radiation is a plane wave. There are two kinds of polarization: horizontal polarization (h-pol) is the radiation whose electric field is perpendicular to the plane of incidence, and vertical polarization (v-pol) is the radiation whose electric field is parallel to the plane of incidence. When the h-pol and v-pol components are equal, the radiation is referred to as unpolarized radiation. On the contrary, when one component is greater than the other, the radiation is called polarized radiation [19].

As far as croplands are concerned, there are three characteristics related to our approach. First, the soil thermal emission right below the soil surface is initially unpolarized because there are many sources randomly oriented and then can be polarized due to the rough soil surface and vegetation canopy where the crops are planted in periodically-spaced rows. It is noted that since we focus on the vegetation scattering effect, the soil surface is treated as the flat surface. Second, the vegetation

scattering generated from plants can also be coherent and polarized radiation in cropland. Third, the resolution of SMAP is 33 km, which indicates there are very large number of plants (scatterers) on the SMAP antenna's footprint.

3.1.2 Periodic Boundary Condition and Floquet Port

In order to account for a given incident plane wave with a polarization and the effects of scattering and coherency from the very large number of plants, we model the vegetation canopy consisting of infinite cylinders as shown in Figure 3.1. The unit cell is comprised of the PBC (periodic boundary condition) and two Floquet ports. The PBC enforces a periodicity in the fields that would exist from this infinitely periodic structure. The Floquet port makes it possible to analyze the infinite periodic structure by confining a computational domain in the unit cell and generates plane waves consisting of TE (traverse electric, h-pol) and TM (traverse magnetic, v-pol) Floquet modes. The S-parameters can be derived by decomposing the fields on the Floquet port into Floquet modes. Thus, we can get S_{11}, S_{22} (reflection coefficients) and S_{12}, S_{21} (transmission coefficients) for each polarization.

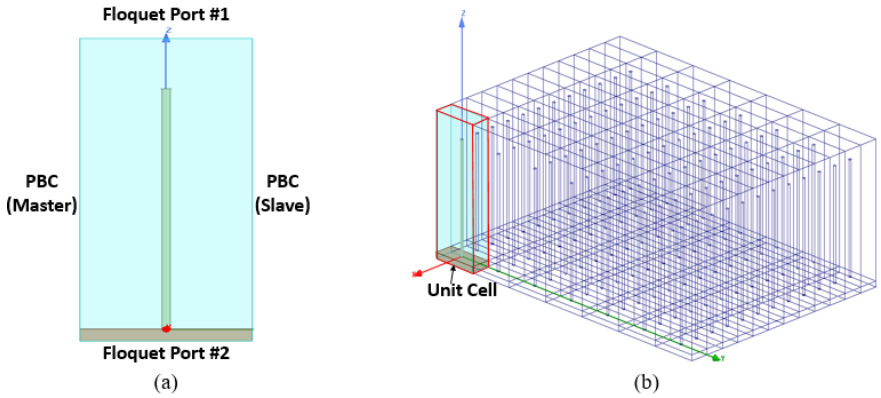

Figure 3.1 HFSS modeling of a vegetation canopy (a) Unit cell with periodic boundary condition and two Floquet ports (b) Planar array with periodicity in x and y-directions.

3.1.3 Plane Wave with Oblique Incidence

We can excite a plane wave with oblique incidence from the Floquet port by using the scan angle technique. The pair of the PBC on the unit cell's vertical walls are consisting of the Master and Slave boundary conditions, and the phase delay can be defined through the slave boundary. Thus, we can enforce the progressive phase delay across the PBC so that a plane wave propagates in the intended scan angle as shown in Figure 3.2.

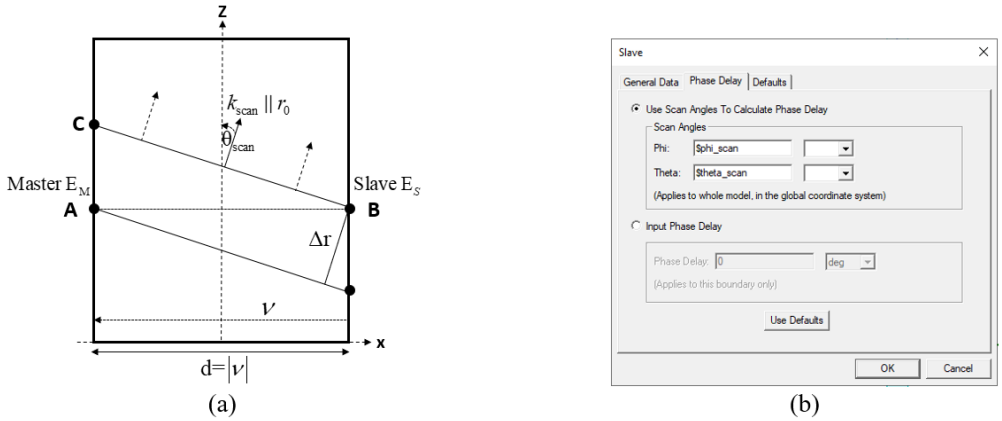

Figure 3.2 (a) A pair of master and slave boundary (b) variation of two scan angles (θ and ϕ) in HFSS [8].

This scan angle technique was explained in detail in [8]. The propagation vector of the radiated wave is given by

$$\vec{k}_{\text{scan}} = k_0 \left[\cos\phi_{\text{scan}} \sin\theta_{\text{scan}},\ \sin\phi_{\text{scan}} \sin\theta_{\text{scan}},\ \cos\theta_{\text{scan}}\right] \tag{3.1}$$

In the AB plane, the radiated fields at the master boundary (point A) and at the slave boundary (point B) are expressed relatively as

$$E_M = E_0 \exp(j\omega t - jk_{\text{scan}} r_0) \tag{3.2}$$

$$\begin{aligned} E_S &= E_0 \exp\left[j\omega t - jk_{\text{scan}}(r_0 + \Delta r)\right] = E_0 \exp\left[j\omega t - jk_{\text{scan}} r_0 - jk_0 \Delta r\right] \\ &= E_M \exp(-jk_0 \Delta r) \end{aligned} \tag{3.3}$$

where k_0 is the free-space wave number ($= \omega\sqrt{\mu_0 \epsilon_0}$), ω is the angular frequency, and ϵ_0 and μ_0 are the permittivity and permeability of free space, respectively.

From the triangle ABC, the phase shift is be obtained by (3.4) and we re-express (3.3) as (3.5).

$$\Delta r = d \sin \theta_{\text{scan}} \tag{3.4}$$

$$E_S = E_M \exp(-jk_0 d \sin \theta_{\text{scan}}) \tag{3.5}$$

The phase shift ($\Delta\Phi$) in degree between master/slave boundaries can be set in relation to the wavelength by

$$\Delta\Phi = \frac{360^\circ \, d \, \sin \theta_{\text{scan}}}{\lambda} \tag{3.6}$$

In addition, the function (Ψ) relating E_S to E_M is described in the HFSS technical notes ("Calculating the E-Field on the Slave Boundary") as (3.7).

$$\Psi = k_0(\vec{r}_0 \cdot \vec{\nu}) = -k_0 d \sin \theta_{\text{scan}} \tag{3.7}$$

$$E_S = E_M \exp(-j\Psi) \tag{3.8}$$

where $\vec{r}_0$ is the unit vector in the scan direction, $\vec{\nu}$ is the vector from the slave boundary to the master boundary. Then, (3.5) and (3.8) coincide with each other. Furthermore, the option of entering the scan angle, θ and ϕ, is given in the HFSS to relate E_S to E_M.

3.2 Floquet Modes in Infinite Periodic Sources

The scattered fields generated by induced currents on an infinite periodic structure can be expressed alternatively as series of Floquet modal functions on the port. The benefit of using the Floquet modal function is to be able to derive the electromagnetic fields in terms of Floquet modes when solving Maxwell's equations. This section illustrates a procedure of how the electric field can be derived from an infinite array of sources in terms of Floquet modes. Additionally, the relationship between a propagating Floquet mode and a unit-cell size is introduced. Formulations in this section follow [10].

3.2.1 Two-Dimensional Floquet Series

An infinite array of sources whose magnitudes are progressive phase shift can be represented in terms of a Floquet series. Suppose a complex function $g(x, y)$ defined as

$$g(x,y) = \sum_{m=-\infty}^{\infty} \sum_{n=-\infty}^{\infty} f(x - x_{mn}, y - y_{mn}) \exp(-jk_{x0}x_{mn} - jk_{y0}y_{mn}) \tag{3.9}$$

where discrete grid points (x_{mn}, y_{mn}) are placed at intervals of a and b relatively on the xy-plane as shown in Figure 3.3. For the rectangular grids, $x_{mn} = ma$ and $y_{mn} = nb$, where m and n are integers varying from $-\infty$ to $+\infty$. k_{x0} and k_{y0} are two constants that determine the progressive phase shift between the nearby cells. In addition, a and b are analogous to the unit cell size in x and y-directions in our modeling.

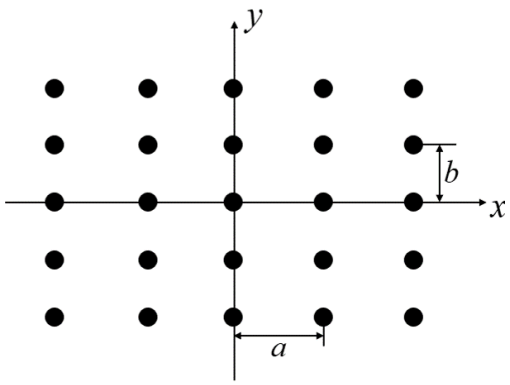

Figure 3.3 Rectangular grid of planar periodic sources.

We use the Fourier transform of $g(x, y)$ to derive the Floquet series expansion of $g(x, y)$. This yields

$$\tilde{g}(k_x, k_y) = \frac{1}{4\pi^2} \int_{-\infty}^{+\infty} \int_{-\infty}^{+\infty} g(x,y) \exp(jk_x x + jk_y y) dx dy \tag{3.10}$$

Using its Fourier transform (3.10), the periodic function $g(x, y)$ can be re-expressed in an alternative format by

$$g(x,y) = \int_{-\infty}^{+\infty} \int_{-\infty}^{+\infty} \tilde{g}(k_x, k_y) \exp(-jk_x x - jk_y y) dk_x dk_y \tag{3.11}$$

Substituting $g(x,y)$ from (3.9) into (3.10), we derive

$$\tilde{g}(k_x,k_y) = \frac{1}{4\pi^2}\sum_{m=-\infty}^{\infty}\sum_{n=-\infty}^{\infty}[\exp(-jk_{x0}x_{mn} - jk_{y0}y_{mn}) \int_{-\infty}^{+\infty}\int_{-\infty}^{+\infty} f(x-x_{mn},\, y-y_{mn})\exp(jk_x x + jk_y y)dxdy] \quad (3.12)$$

Substituting $x' = x - x_{mn}$ and $y' = y - y_{mn}$, we have

$$\tilde{g}(k_x,k_y) = \tilde{f}(k_x,k_y)\sum_{m=-\infty}^{\infty}\sum_{n=-\infty}^{\infty}\exp\left[jx_{mn}(k_x-k_{x0}) + jy_{mn}(k_y-k_{y0})\right] \quad (3.13)$$

where $\tilde{f}(k_x,k_y)$ is the Fourier transform of $f(x,y)$

$$\tilde{f}(k_x,k_y) = \frac{1}{4\pi^2}\int_{-\infty}^{+\infty}\int_{-\infty}^{+\infty} f(x',y')\exp(jk_x x' + jk_y y')dx'dy'$$

We focus on a double summation term in (3.13). Using the expressions $x_{mn} = ma$ and $y_{mn} = nb$, we can re-express the double-summation term as

$$\begin{aligned} S &= \sum_{m=-\infty}^{\infty}\sum_{n=-\infty}^{\infty}\exp\left[jx_{mn}(k_x-k_{x0}) + jy_{mn}(k_y-k_{y0})\right] \\ &= \sum_{m=-\infty}^{\infty}\exp\left[jma(k_x-k_{x0})\right]\sum_{n=-\infty}^{\infty}\exp\left[jnb(k_y-k_{y0})\right] \end{aligned} \quad (3.14)$$

The infinite series in (3.14) can be also represented by the following infinite series of Dirac delta functions (3.15). The details for derivation are given in Appendix A.

$$S = \frac{2\pi}{a}\sum_{m=-\infty}^{\infty}\delta(k_x - k_{x0} - \frac{2m\pi}{a})\sum_{n=-\infty}^{\infty}\delta(k_y - k_{y0} - \frac{2n\pi}{b}) \quad (3.15)$$

Substituting (3.15) into the summation part in (3.13), we finally get the Fourier transform for $g(x,y)$ as

$$\tilde{g}(k_x,k_y) = \frac{4\pi^2}{ab}\tilde{f}(k_x,k_y)\sum_{m=-\infty}^{\infty}\sum_{n=-\infty}^{\infty}\delta(k_x - k_{x0} - \frac{2m\pi}{a})\delta(k_y - k_{y0} - \frac{2n\pi}{b}) \quad (3.16)$$

Due to the Dirac delta function in (3.16), $\tilde{g}(k_x,k_y)$, the Fourier spectrum for $g(x,y)$, become zero everywhere except at discrete points as

$$k_x = k_{xmn} = k_{x0} + \frac{2m\pi}{a} \qquad k_y = k_{ymn} = k_{y0} + \frac{2n\pi}{b} \quad (3.17)$$

Substituting $\tilde{g}(k_x, k_y)$ from (3.16) into (3.11), we finally obtain $g(x, y)$ in terms of a series of complex exponential function as

$$g(x,y) = \frac{4\pi^2}{ab} \sum_{m=-\infty}^{\infty} \sum_{n=-\infty}^{\infty} \tilde{f}(k_{xmn}, k_{ymn}) \exp(-jk_{xmn}x - jk_{ymn}y) \tag{3.18}$$

The right-hand side of (3.18) is the Floquet series expansion of $g(x, y)$ where k_{xmn} and k_{ymn} are defined in (3.17), and $a \times b$ is the unit cell size.

3.2.2 Two-Dimensional Floquet Excitation

As presented in the previous subsection, we obtained Floquet series expansions of a periodic function (3.9) for two-dimensional case with rectangular grid structure. We will derive the electromagnetic fields generated by planar periodic sources expressed by (3.18), and the electromagnetic field will be expressed in terms of Floquet modal functions.

The surface current excitation function located on the xy-plane can be expressed as

$$\vec{I}(x,y) = \hat{y} \sum_{m=-\infty}^{\infty} \sum_{n=-\infty}^{\infty} f(x - x_{mn}, y - y_{mn}) \exp(-jk_{x0}x_{mn} - jk_{y0}y_{mn}) \tag{3.19}$$

where $x_{mn} = ma$ and $y_{mn} = nb$.

The surface current above will generate the TM_y field, which is referred to as the transverse magnetic field to y-axis. Also, the TM_y fields can be derived by solving a scalar Helmholtz equation in free space (3.20) where the magnetic vector potential ($\vec{A}$) holds $\vec{H} = \nabla \times \vec{A}$.

$$\nabla^2 A_y + k_0^2 A_y = -J_y \tag{3.20}$$

The y-component of the volume current density J_y in (3.20) can be obtained by introducing a Dirac delta function to the surface current density in (3.19) as follows:

$$\nabla^2 A_y + k_0^2 A_y = -\delta(z) \sum_{m=-\infty}^{\infty} \sum_{n=-\infty}^{\infty} f(x - x_{mn}, y - y_{mn}) \exp(-jk_{x0}x_{mn} - jk_{y0}y_{mn}) \tag{3.21}$$

We can re-express the right-hand side in (3.21) in terms of Floquet series by following the same procedure used in subsection 3.2.1 such that we can find a solution for A_y conveniently. This yields

$$\nabla^2 A_y + k_0^2 A_y = -\delta(z) \frac{4\pi^2}{ab} \sum_{m=-\infty}^{\infty} \sum_{n=-\infty}^{\infty} \tilde{f}(k_{xmn}, k_{ymn}) \exp(-jk_{xmn}x - jk_{ymn}y) \tag{3.22}$$

Inspecting the right-hand side of (3.22) makes us to assume a solution of A_y as follows:

$$A_y = \sum_{m=-\infty}^{\infty} \sum_{n=-\infty}^{\infty} F_{mn}(z) \exp(-jk_{xmn}x - jk_{ymn}y) \tag{3.23}$$

We can find the unknown function $F_{mn}(z)$ by substituting A_y in (3.23) into (3.22) and then comparing each term. This yields

$$\frac{\partial^2 F_{mn}(z)}{\partial z^2} + k_{zmn}^2 F_{mn}(z) = -\delta(z)\frac{4\pi^2}{ab}\tilde{f}(k_{xmn}, k_{ymn}) \tag{3.24}$$

$$k_{zmn}^2 = k_0^2 - k_{xmn}^2 - k_{ymn}^2 \tag{3.25}$$

General solution to (3.24) when $z \neq 0$ is

$$F_{mn}(z) = A_{mn} \exp(-jk_{zmn}|z|) \tag{3.26}$$

In order to find the unknown coefficient A_{mn}, we can use a property of the Dirac delta function by integrating both sides in (3.24) over a interval $-\epsilon/2 < z < \epsilon/2$ where ϵ is near-zero value. This yields

$$A_{mn} = \frac{2\pi^2}{jabk_{zmn}}\tilde{f}(k_{xmn}, k_{ymn}) \tag{3.27}$$

Substituting A_{mn} in (3.27) into (3.26), $F_{mn}(z)$ in the $z > 0$ region can be re-expressed by

$$F_{mn}(z) = \frac{2\pi^2}{jabk_{zmn}}\tilde{f}(k_{xmn}, k_{ymn}) \exp(-jk_{zmn}z) \tag{3.28}$$

Finally we can derive A_y in (3.23) as

$$A_y = \sum_{m=-\infty}^{\infty} \sum_{n=-\infty}^{\infty} \frac{2\pi^2}{jabk_{zmn}}\tilde{f}(k_{xmn}, k_{ymn}) \exp(-jk_{zmn}z - jk_{xmn}x - jk_{ymn}y) \tag{3.29}$$

The electromagnetic fields can be derived by solving the following Maxwell's equations:

$$\vec{H} = \nabla \times (\hat{y}A_y), \quad \vec{E} = \frac{1}{j\omega\epsilon_0}\nabla \times \vec{H} \tag{3.30}$$

From (3.30), we derive the electric fields for the $z > 0$ region as

$$E_x = \frac{2\pi^2}{ab\omega\epsilon_0} \sum_{m=-\infty}^{\infty} \sum_{n=-\infty}^{\infty} \frac{k_{xmn}k_{ymn}}{k_{zmn}}\tilde{f}(k_{xmn}, k_{ymn}) \exp[-j(k_{xmn}x + k_{ymn}y + k_{zmn}z)] \tag{3.31a}$$

$$E_y = -\frac{2\pi^2}{ab\omega\epsilon_0} \sum_{m=-\infty}^{\infty} \sum_{n=-\infty}^{\infty} \frac{k_0^2 - k_{ymn}^2}{k_{zmn}}\tilde{f}(k_{xmn}, k_{ymn}) \exp[(-j(k_{xmn}x + jk_{ymn}y + jk_{zmn}z)] \tag{3.31b}$$

$$E_z = \frac{2\pi^2}{ab\omega\epsilon_0} \sum_{m=-\infty}^{\infty} \sum_{n=-\infty}^{\infty} k_{ymn}\tilde{f}(k_{xmn}, k_{ymn}) \exp[-j(k_{xmn}x + jk_{ymn}y + jk_{zmn}z)] \tag{3.31c}$$

Thus, the electric fields generated by planar periodic sources in (3.19) are represented in terms of an infinite series. Also, the exponential term inside the double summation is referred to as a Floquet modal function or a Floquet mode. Furthermore, it is shown that the the propagation direction of TM_{ymn} Floquet mode is parallel to the vector $\vec{k}_{mn}$ as follows:

$$\vec{k}_{mn} = \hat{x}k_{xmn} + \hat{y}k_{ymn} + \hat{z}k_{zmn} \tag{3.32}$$

The radiation angle (θ_{mn}, ϕ_{mn}) corresponding to the vector $\vec{k}_{mn}$ in the spherical coordinate is

$$k_{xmn} = k_0 \sin\theta_{mn} \cos\phi_{mn} \tag{3.33a}$$

$$k_{ymn} = k_0 \sin\theta_{mn} \sin\phi_{mn} \tag{3.33b}$$

$$k_{zmn} = k_0 \cos\theta_{mn} \tag{3.33c}$$

It is noted that from (3.17), (3.32) and (3.33) the direction of propagation is related to the (m, n) Floquet mode as shown in Figure 3.4. For example, the zeroth order Floquet mode TM_{00}, called the dominant mode, propagates along our scan angle (θ_0, ϕ_0), and the plane wave with the scan angle (θ_0, ϕ_0) can be obtained from (3.17) and (3.33) by setting $m = n = 0$. This yields

$$k_{x0} = k_0 \sin\theta_0 \cos\phi_0 \tag{3.34a}$$

$$k_{y0} = k_0 \sin\theta_0 \sin\phi_0 \tag{3.34b}$$

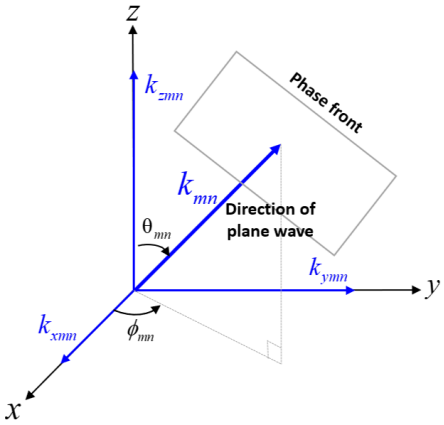

Figure 3.4 Plane wave associated with the (m, n) Floquet mode.

If k_{zmn} in (3.25) is real, the associated Floquet mode, called the propagation mode, propagates unattenuated in the unit cell. In contrast, if k_{zmn} is imaginary, such a Floquet mode, called the evanescent mode, decays along the z-direction.

Additionally, since k_{zmn} is a function of a and b, we can take control of the number of the propagation modes and evanescent modes by adjusting the unit-cell size. For example, if the condition is follows:

$$a \leq \frac{1}{2}\lambda_0 \qquad b \leq \frac{1}{2}\lambda_0 \tag{3.35}$$

only the dominant modes propagate in the intended direction, and the rest become evanescent modes as shown in Figure 3.5. The details for the derivation are given in Appendix B.

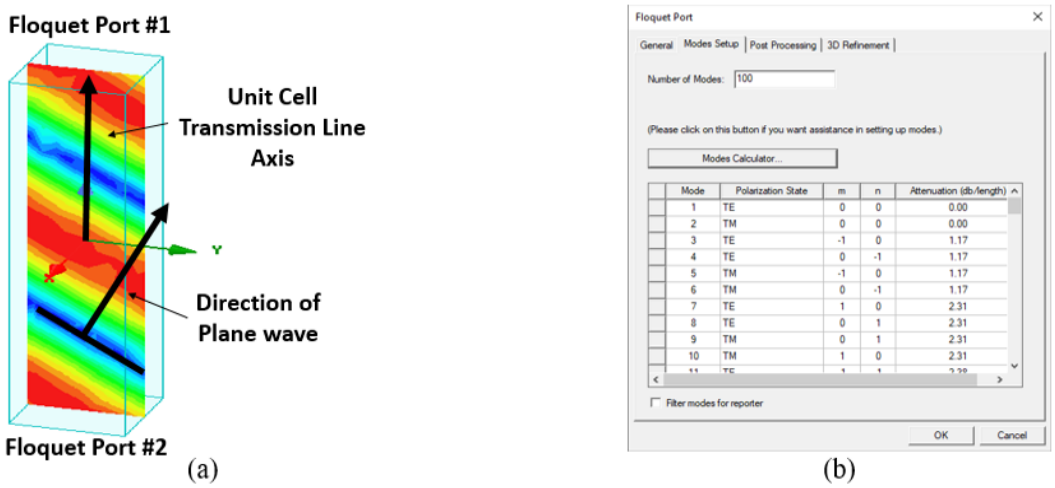

Figure 3.5 Plane wave propagating in a given direction in the unit cell (a) Field overlays of the dominant mode with scan angle (θ_0, ϕ_0)=(40°, 90°) (b) Floquet port modes setup.

In the context of our modeling, the unit-cell size is fixed depending on the cropland because a and b can represent the spacing between plants. There is a chance that non zeroth Floquet mode, which propagates in the unintended direction, can be the propagation mode. Thus, it is necessary to include all the propagation modes and exclude the non-zero attenuation modes in the HFSS Floquet port modes setup in order to increase simulation efficiency and ease interpretation of the S-parameters of interests.

3.3 Unit Cell Analysis of Infinite Array

The analysis of infinite structure is accomplished by solving a unit cell. Because the computational domain is restricted to the unit cell, we can take advantage of developing a fast and efficient approach to calculate S-parameters. Also, the unit cell analysis accounts for the array factor determined by the array's lattice and progressive phase shift. This section illustrates how the array factor will be derived and interprets S-parameters.

3.3.1 Array Factor

The benefit of accounting for array factor in the unit cell analysis makes it possible for us to account for the coherency of vegetation scattering. The formulations of the array factor in this subsection follow [10].

The far field of the infinite periodic sources along our intended direction, $\vec{E}_\infty(r,\theta,\phi)$, is derived by multiplying the array factor by the element pattern. This yields,

$$\vec{E}_\infty(r,\theta,\phi) = \mathrm{AF}_0(\theta,\phi)\vec{E}_a(\theta,\phi)\frac{\exp(-jk_0r)}{r} \tag{3.36}$$

where $\vec{E}_a(\theta,\phi)\exp(-jk_0r)/r$ is the active element far-field pattern, and the elements are arrayed as shown in Figure 3.3. Here, we focus on the array factor AF_0.

Assuming the field associated with the Floquet dominant mode radiates in the (θ_0,ϕ_0)-direction, the phase gradients k_{x0} and k_{y0} are expressed as (3.34). Also, using the expressions $x_{mn} = ma$ and $y_{mn} = nb$, we can express the array factor for uniform excitation as

$$\begin{aligned}\mathrm{AF}(\theta,\phi) &= \sum_{m=-\infty}^{\infty}\sum_{n=-\infty}^{\infty}\exp\left[jx_{mn}(k_x-k_{x0})+jy_{mn}(k_y-k_{y0})\right] \\ &= \sum_{m=-\infty}^{\infty}\exp\left[jma(k_x-k_{x0})\right]\sum_{n=-\infty}^{\infty}\exp\left[jnb(k_y-k_{y0})\right]\end{aligned} \tag{3.37}$$

where

$$k_x = k_0\sin\theta\cos\phi \qquad k_y = k_0\sin\theta\sin\phi \tag{3.38}$$

Using the identity described in the Appendix A, The array factor can be re-expressed by

$$\mathrm{AF}(\theta,\phi) = \frac{4\pi^2}{ab}\sum_{m=-\infty}^{\infty}\sum_{n=-\infty}^{\infty}\delta\left(k_x-k_{x0}-\frac{2m\pi}{a}\right)\delta\left(k_y-k_{y0}-\frac{2n\pi}{b}\right) \tag{3.39}$$

Due to the Dirac delta functions in (3.39), the array factor only exhibits at discrete angles. Also, since the radiation field associated with the dominant mode propagates along our intended direction (θ_0, ϕ_0), the array factor in our intended direction can be expressed by

$$\mathrm{AF}_0(\theta, \phi) = \frac{4\pi^2}{ab}\delta(k_x - k_{x0})\delta(k_y - k_{y0}) \tag{3.40}$$

Again, in the context of our modeling, the array factor can represent the mutual coupling between the scattered field of the infinite cylinder. In addition, it contributes to not only the far field intensity in (3.36) but also S-parameters.

3.3.2 Interpretation of S-parameters

3.3.2.1 Basic Concept of Decomposing the Scattered Field

The S-parameters are obtained by decomposing the fields on the Floquet port into Floquet modes [26]. Let us assume that the scattered field, E_z^s, in the top surface of the unit cell, $z = z_0$, can be represented in terms of infinite series of Floquet modes as

$$E_z^s = \sum_{m=-\infty}^{\infty}\sum_{n=-\infty}^{\infty} e_{mn}\exp(-jk_{xmn}x - jk_{ymn}y - jk_{zmn}z_0) \tag{3.41}$$

where e_{mn} is an amplitude of each Floquet mode, $k_{xmn} = k_x + 2m\pi/a$, and $k_{ymn} = k_y + 2n\pi/b$.

The reflection coefficient of the scattered field (3.41) can be obtained by multiplying both sides by $\exp(jk_{xm'n'}x + jk_{ym'n'}y)$ and then integrating in a full period of the unit-cell size $a \times b$. Since the Floquet modes are orthogonal to each other over the period along the x- and y-directions, we can obtain the simplified equation as

$$\int_{x=0}^{a}\int_{y=0}^{b} E_z^s(x, y, z_0)\exp(jk_{xm'n'}x + jk_{ym'n'}y)dxdy = e_{m'n'}\, a\, b\, \exp(-jk_{zm'n'}z_0) \tag{3.42}$$

From (3.42), one obtains

$$e_{mn} = \frac{\exp(jk_{zmn}z_0)}{ab}\int_{x=0}^{a}\int_{y=0}^{b} E_z^s(x, y, z_0)\exp(jk_{xmn}x + jk_{ymn}y)dxdy \tag{3.43}$$

Thus, the magnitude of reflection coefficient of the zeroth Floquet mode (the dominant mode) can be expressed as

$$R_0 = e_{00}/E_0 \tag{3.44}$$

It is noted that R_0 can represent the Fresnel reflection coefficient for the case of air and soil in the context of our modeling if there exists only the zeroth order Floquet mode in the unit cell. Furthermore, this method can allow us to observe the reflection and transmission coefficients for the multilayered case.

3.3.2.2 Generalized Scattering Matrix

The HFSS solution provides us the scattering parameters regarding to the infinite array structure by applying a Floquet modal decomposition technique. The S-parameters are cast in the form of a Generalized Scattering Matrix (GSM) interrelating the Floquet modes. The conceptual illustration of the GSM is described here.

The GSM is derived as the relation between incident and reflected voltages associated with the Floquet mode, as shown in Figure 3.6, where a_{mn} and b_{mn} are the incident voltage vectors at the two Floquet ports and c_{mn} and d_{mn} are the reflected voltage vectors corresponding to a_{mn} and b_{mn}. The S-matrix is a 4×4 matrix and interrelates the TE_z (h-pol) and TM_z (v-pol) Floquet modes where S_{11} and S_{22} are the reflection coefficients, S_{12} and S_{21} are the transmission coefficients. Also, the coupling effect with two different polarizations is given in the GSM [10].

The HFSS solution in Figure 3.6 is also given as an example of the S-matrix to help the interpretation. First, the Floquetport 1:1 refers to the TE_{00} mode and the Floquetport 1:2 refers to the TM_{00} mode from the Floquet port 1. Second, the forth entry of the second column indicates that 0.7528 is the magnitude of the TM_{00} transmission coefficient of the unit cell from the port 1 to the port 2. Third, the first entry of the fourth column shows that the coupling between TE_{00} mode and TM_{00} mode, 0.0004, is small enough to be negligible.

In the conclusion, we can obtain different S-parameters depending on the soil and cylinder electric properties (permittivity, permeability, and conductivity), the unit-cell size $a \times b$, and the dimension of cylinder. It is noted that the unit-cell size describes the regularly spacing between rows of plants in the cropland, and the dimension of cylinder represents a plant. By utilizing S-parameters, we can observe not only the reflection and transmission coefficients but also trans-

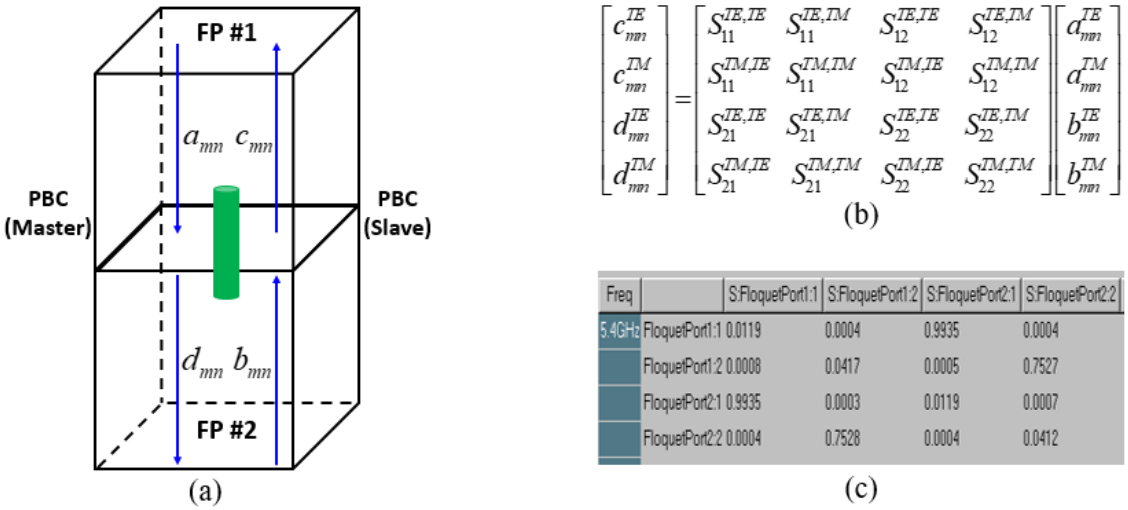

Figure 3.6 (a) Configuration of the unit cell showing Floquet Port (FP) and the incident and reflected voltage vectors (b) Generalized scattering matrix (4×4) [9] (c) HFSS solution.

missivity of the vegetation canopy as a function of the frequency and observed angles, which will be discussed in Chapter 4.

CHAPTER 4. SIMULATION RESULTS

This chapter includes simulation results based on our proposed approach introduced in the Chapter 3. We first simulated for the simple case of a 2-layer case (soil and air) in order to observe the reflection and transmission coefficients. Also, by adding the vegetation canopy on top of the soil layer, we were able to observe the vegetation scattering effect. In addition, the vegetation canopy case consisting of an infinite number of finite-length cylinder without soil was simulated in order to get the transmissivity that is directly related to the vegetation optical depth.

4.1 Reflection and Transmission for 2-layer Composite: Soil and Air

The Fresnel reflectivity $|S_{11}|^2$ and transmissivity $|S_{21}|^2$ are computed by using two approaches; HFSS and analytical solution, and we compare each other to validate our model. Two cases are considered; one is for the wave propagating downward from air to soil, and the other is for the wave propagating upward from soil to air. In this way, we observe how much power is reflected and transmitted through the boundary as well as the Brewster angle and critical angle.

4.1.1 Soil Property

As mentioned in Chapter 1, the soil in the South Fork located in Iowa is classified by loam and silty clay loam. Thus, we assume that the soil relative complex permittivity is $\tilde{\epsilon}_{r,\text{soil}} = 18 - j3$ at 1.41 GHz when the volumetric moisture m_v is 0.3% [27]. For the lossless soil case, the soil permittivity is treated as $\epsilon_{r,\text{soil}} = 18$ without the imaginary part. In addition, it is noted that relative complex permittivity $\tilde{\epsilon}_r (= \epsilon_r' - j\epsilon_r'')$ is defined as

$$\epsilon_r' = \epsilon_r \qquad \epsilon_r'' = \frac{\sigma}{\omega \epsilon_0} \tag{4.1}$$

where ϵ_r is the dielectric constant, σ is the conductivity, and $\epsilon (= \epsilon_0 \tilde{\epsilon}_r)$ is the complex permittivity.

Also, the soil propagation constant γ_{soil} and intrinsic impedance η_{soil} are defined as

$$\gamma_{\text{soil}} = \alpha_{\text{soil}} + j\beta_{\text{soil}} \qquad \eta_{\text{soil}} = \sqrt{\frac{j\omega\mu_0}{j\omega\epsilon_{\text{soil}} + \sigma_{\text{soil}}}} \tag{4.2}$$

with

$$\alpha_{\text{soil}} = \omega\sqrt{\mu_0\epsilon_{\text{soil}}}\sqrt{\frac{1}{2}\left[\sqrt{1+\left(\frac{\sigma_{\text{soil}}}{\omega\epsilon_{\text{soil}}}\right)^2} - 1\right]} \tag{4.3}$$

$$\beta_{\text{soil}} = \omega\sqrt{\mu_0\epsilon_{\text{soil}}}\sqrt{\frac{1}{2}\left[\sqrt{1+\left(\frac{\sigma_{\text{soil}}}{\omega\epsilon_{\text{soil}}}\right)^2} + 1\right]} \tag{4.4}$$

where α_{soil} is the attenuation constant (Np/m), and β_{soil} is the phase constant (rad/m).

4.1.2 Mathematical Formula for Each Polarization

The Fresnel reflection coefficient R and transmission coefficient T can be expressed in terms of the propagation constant γ, the impedance η, and admittance y toward the z direction such that we can reduce the error regarding to the root of negative numbers in the context of coding in the MATLAB.

When the polarized uniform wave propagating in medium 1 is incident at an oblique angle on the boundary of two media with distinct electrical properties, the wave is scattered. Some wave is reflected back into medium 1; the rest of the wave is transmitted through medium 2. The general expressions for this case are as follows:

For the horizontal polarization (h-pol),

$$\eta_{iz} = \frac{j\omega\mu_i}{\gamma_{iz}} = \frac{\eta_i}{\cos\theta_i} \tag{4.5}$$

$$R_{12}^h = \frac{\eta_2\cos\theta_1 - \eta_1\cos\theta_2}{\eta_2\cos\theta_1 + \eta_1\cos\theta_2} = \frac{\eta_{2z} - \eta_{1z}}{\eta_{2z} + \eta_{1z}} = \frac{\mu_2\gamma_{1z} - \mu_1\gamma_{2z}}{\mu_2\gamma_{1z} + \mu_1\gamma_{2z}} \tag{4.6}$$

$$T_{21}^h = \frac{2\eta_2\cos\theta_1}{\eta_2\cos\theta_1 + \eta_1\cos\theta_2} = \frac{\eta_{2z}}{\eta_{2z} + \eta_{1z}} = \frac{2\mu_2\gamma_{1z}}{\mu_2\gamma_{1z} + \mu_1\gamma_{2z}} \tag{4.7}$$

For the vertical polarization (v-pol),

$$\eta_{iz} = \frac{\gamma_{iz}}{j\omega\epsilon_i} = \eta_i \cos\theta_i, \qquad y_{iz} = \frac{j\omega\epsilon_i}{\gamma_{iz}} = \frac{1}{\eta_{iz}} \tag{4.8}$$

$$R_{12}^v = \frac{\eta_1 \cos\theta_1 - \eta_2 \cos\theta_2}{\eta_1 \cos\theta_1 + \eta_2 \cos\theta_2} = \frac{y_{2z} - y_{1z}}{y_{2z} + y_{1z}} = \frac{\epsilon_2\gamma_{1z} - \epsilon_1\gamma_{2z}}{\epsilon_2\gamma_{1z} + \epsilon_1\gamma_{2z}} \tag{4.9}$$

$$T_{21}^v = \frac{2\eta_1 \cos\theta_1}{\eta_1 \cos\theta_1 + \eta_2 \cos\theta_2} = \frac{2y_{2z}}{y_{2z} + y_{1z}} = \frac{2\epsilon_2\gamma_{1z}}{\epsilon_2\gamma_{1z} + \epsilon_1\gamma_{2z}} \tag{4.10}$$

For the phase matching,

$$(\alpha_1 + j\beta_1)\sin\theta_1 = \gamma_1 \sin\theta_1 = \gamma_2 \sin\theta_2 = (\alpha_2 + j\beta_2)\sin\theta_2 \qquad \text{(Snell's law)} \tag{4.11}$$

For the Brewster angle θ_B and critical angle θ_c,

$$\theta_B = \tan^{-1}(\sqrt{\epsilon_2/\epsilon_1}) \qquad \text{only for v-pol} \tag{4.12}$$

$$\theta_c = \sin^{-1}(\sqrt{\epsilon_2/\epsilon_1}) \qquad \text{for h-pol and v-pol} \tag{4.13}$$

where Brewster angle θ_B is defined as the incident angle which reduces the reflection coefficient for v-pol to zero. The critical angle θ_c is the incident angle, which allows total reflection for h-pol and v-pol and exists if the wave propagates from a denser medium to a less dense medium.

In order to compare the S-parameters in HFSS, we need to derive the analytical solution for the incident power P_{inc} and the transmitted power P_{trm} for each polarization. The general expressions are as follows:

For the horizontal polarization (h-pol) and non-magnetic materials,

$$P_{\text{inc}} = \frac{1}{2}\,\text{Re}\left[E_{1y}^i H_{1x}^{i^*}\right] = \frac{1}{2}\,\text{Re}\left[\frac{1}{\eta_{1z}^*}|E_0|^2\right] = \frac{1}{2}\,\text{Re}\left[\frac{1}{\eta_{1z}}\right]|E_0|^2 = \frac{\text{Re}[\eta_{1z}]}{2|\eta_{1z}|^2}|E_0|^2 \tag{4.14}$$

$$P_{\text{trm}} = \frac{1}{2}\,\text{Re}\left[E_{2y}H_{2x}^*\right] = \frac{\text{Re}[\eta_{2z}]}{2|\eta_{2z}|^2}|T_{21}^h E_0|^2 \tag{4.15}$$

$$|S_{21}|^2 = \frac{P_{\text{trm}}}{P_{\text{inc}}} = \frac{\text{Re}[1/\eta_{2z}]}{\text{Re}[1/\eta_{1z}]}|T_{21}^h|^2 = |T_{21}^h|^2\,\text{Re}\left[\frac{\cos\theta_2}{\eta_2}\right]\Big/\text{Re}\left[\frac{\cos\theta_1}{\eta_1}\right] = \frac{\text{Im}[\gamma_{2z}]}{\text{Im}[\gamma_{1z}]}|T_{21}^h|^2 \tag{4.16}$$

$$|S_{11}|^2 = \frac{P_{\text{ref}}}{P_{\text{inc}}} = |R_{12}^h|^2 \tag{4.17}$$

For the vertical polarization (v-pol) and non-magnetic materials,

$$P_{\text{inc}} = \frac{1}{2}\,\text{Re}\left[E^i_{1x}H^{i*}_{1y}\right] = \frac{1}{2}\,\text{Re}[\eta_{1z}]|H_0|^2 \tag{4.18}$$

$$P_{\text{trm}} = \frac{1}{2}\,\text{Re}\left[E_{2x}H^{*}_{2y}\right] = \frac{1}{2}\,\text{Re}[\eta_{2z}]|T^v_{21}H_0|^2 \tag{4.19}$$

$$|S_{21}|^2 = \frac{P_{\text{trm}}}{P_{\text{inc}}} = \frac{\text{Re}[\eta_{2z}]}{\text{Re}[\eta_{1z}]}|T^v_{21}|^2 = \frac{\text{Im}\left[\gamma_{2z}/\epsilon_2\right]}{\text{Im}\left[\gamma_{1z}/\epsilon_1\right]}|T^v_{21}|^2 \tag{4.20}$$

$$|S_{11}|^2 = \frac{P_{\text{ref}}}{P_{\text{inc}}} = |R^v_{12}|^2 \tag{4.21}$$

4.1.3 Wave Propagating Downward from Air to Soil

Figure 4.1 shows that a wave propagates downward from medium (air) to medium (soil) for each polarization with an incidence angle θ_1. We observe how much power is reflected into air and transmitted into soil.

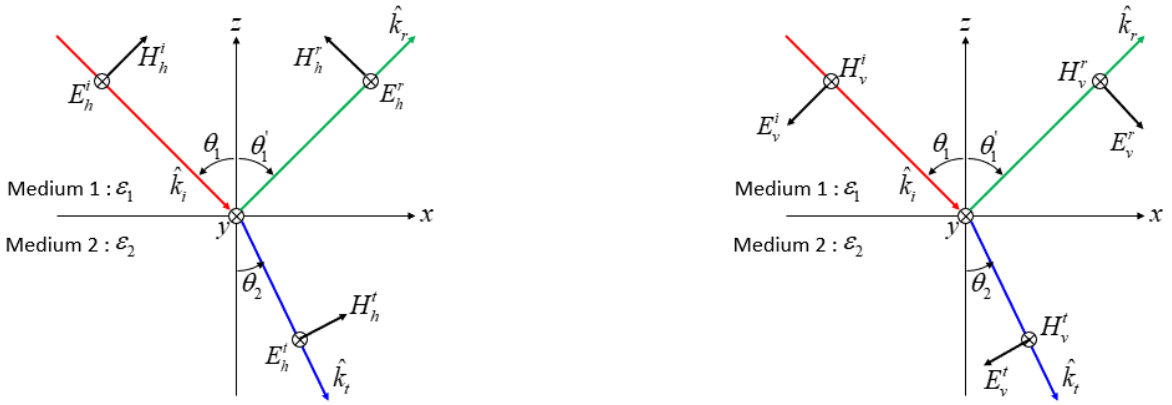

(a) Horizontal Polarization (h-pol, TE_z)

(b) Vertical Polarization (v-pol, TM_z)

Figure 4.1 Polarized plane wave incident at an oblique incidence angle on a surface where medium 1 is air, and medium 2 is soil.

4.1.3.1 Lossless Soil and Air

The 2-layer case (lossless soil and air) is modeled as shown in Figure 4.2 where the operation frequency is 1.41 GHz, the unit-cell size is 10 cm × 10 cm, the depth of soil is 9.6 cm, the same as skin depth ($\delta = 1/\alpha_{soil}$), the height of air is 42 cm ($2\lambda_0$).

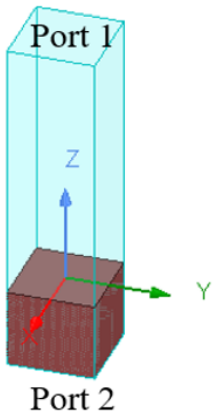

Figure 4.2 The unit cell consisting of air and soil. Radiation propagates from port 1 to port 2.

Figure 4.3 shows that the results of the two approaches are in good agreement. Also, at the Brewster angle (76.7°), the v-pol is totally transmitted into the soil, and only the h-pol is reflected by the surface.

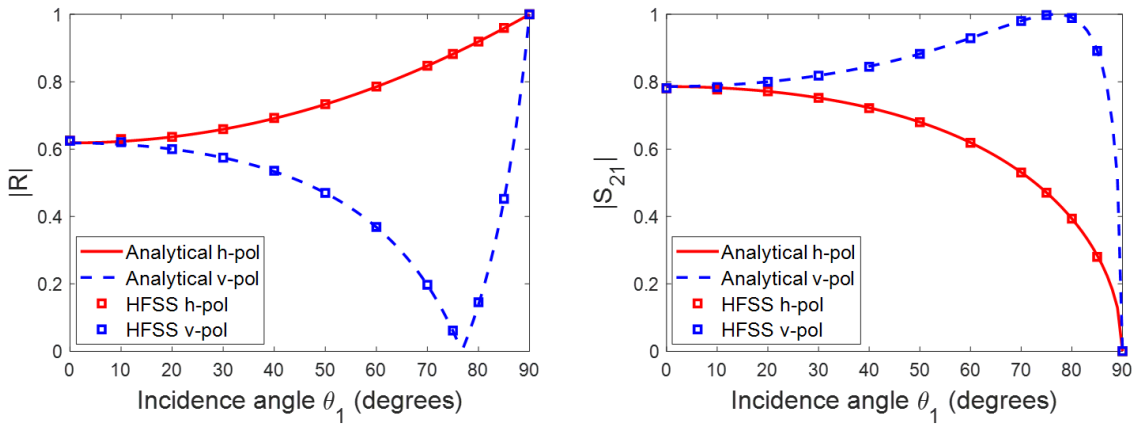

Figure 4.3 Reflection coefficient $|R|$ and transmission coefficient $|S_{21}|$ of the 0th-order Floquet mode for the case of lossless soil when the wave propagates downward.

Figure 4.4 shows that the law of energy conservation is satisfied because there is no energy loss inside the lossless soil. Also, it is noted that $|S_{21}|$ at the boundary is the same as $|S_{21}|$ at port 2.

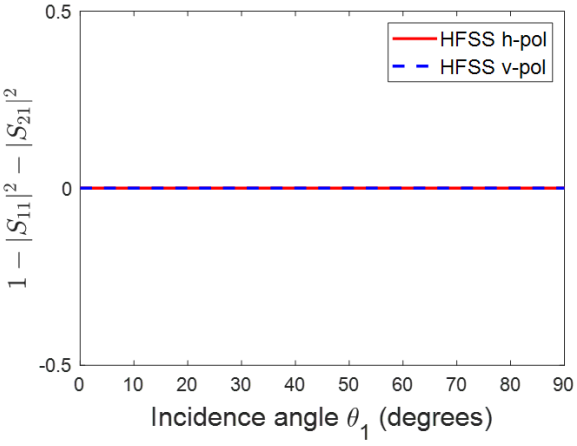

Figure 4.4 Energy conservation as a function of an incidence angle for each polarization.

4.1.3.2 Lossy Soil and Air

Modeling a 2-layer case (lossy soil and air) is the same as the 2-layer case (lossless soil and air), except the soil permittivity is $\tilde{\epsilon}_{r2} = 18 - j3$. The imaginary part of $\tilde{\epsilon}_{r2}$ causes energy loss in soil. Thus, deembedding formula for the analytical solution is required in order to compare with the S_{21} at the port 2.

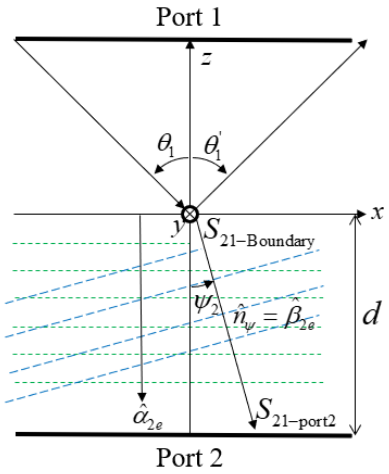

Figure 4.5 Nonuniform plane wave inside the lossy soil where blue and green dash lines indicate constant phase planes and amplitude planes, respectively.

As shown in Figure 4.5, the wave propagating downward in the lossy soil is a nonuniform plane wave with constant phase planes perpendicular to $\vec{n}_\psi$, and constant amplitude planes are parallel to the interface. Also, the wave travels along $\vec{n}_\psi$, whereas its magnitude is attenuated along the z-direction.

The transmitted wave in Figure 4.5 is expressed as

$$\begin{aligned}\vec{E}^t &= \vec{E}_2\, e^{\alpha_{2e} z}\, \exp[-j\beta_{2e}(x\sin\psi_2 - z\cos\psi_2)] \\ &= \vec{E}_2\, e^{\alpha_{2e} z}\, \exp[-j\beta_{2e}(\vec{n}_\psi \cdot \vec{r})]\end{aligned} \tag{4.22}$$

with

$$\cos\theta_2 = \left[1 - \left(\frac{j\beta_1}{\alpha_2 + j\beta_2}\sin\theta_1\right)^2\right]^{1/2} \tag{4.23}$$

$$\alpha_{2e} = \alpha_2\,\mathrm{Re}[\cos\theta_2] - \beta_2\,\mathrm{Im}[\cos\theta_2], \qquad q = \alpha_2\,\mathrm{Im}[\cos\theta_2] + \beta_2\,\mathrm{Re}[\cos\theta_2] \tag{4.24}$$

$$\beta_{2e} = \sqrt{(\beta_1\sin\theta_1)^2 + q^2}, \qquad \psi_2 = \tan^{-1}(\beta_1\sin\theta_1/q) \tag{4.25}$$

where α_{2e} is the effective attenuation constant, β_{2e} is the effective phase constant, and ψ_2 is the real angle [28]. Therefore, the deembedding formula is established as follows:

$$S_{21,\mathrm{port2}} = e^{-\alpha_{2e} d}\, S_{21,\mathrm{boundary}} \tag{4.26}$$

Finally, the analytical solutions for the $|S_{21}|^2$ at the port 2 and $|S_{11}|^2$ at the port 1 are computed as

$$|S_{11}|^2 = \frac{P^r}{P^i} = |R_{12}|^2 \qquad \text{for v-pol and h-pol} \tag{4.27}$$

$$\begin{aligned}|S_{21}|^2 &= e^{-2\,\alpha_{2e} d}\,\frac{\mathrm{Im}[\gamma_{2z}]}{\mathrm{Im}[\gamma_{1z}]}|T_{21}^h|^2 \qquad \text{for h-pol} \\ &= e^{-2\,\alpha_{2e} d}\,\frac{\mathrm{Im}\,[\gamma_{2z}/\epsilon_2]}{\mathrm{Im}\,[\gamma_{1z}/\epsilon_1]}|T_{21}^v|^2 \qquad \text{for v-pol}\end{aligned} \tag{4.28}$$

Figure 4.6 shows that the results of the two approaches are in good agreement. Also, it is observed that due to the imaginary part of the soil permittivity, the v-pol is not totally transmitted into the soil at the Brewster angle (76°), and the $|S_{21}|$ for the lossy soil case is less than that of the lossless soil case.

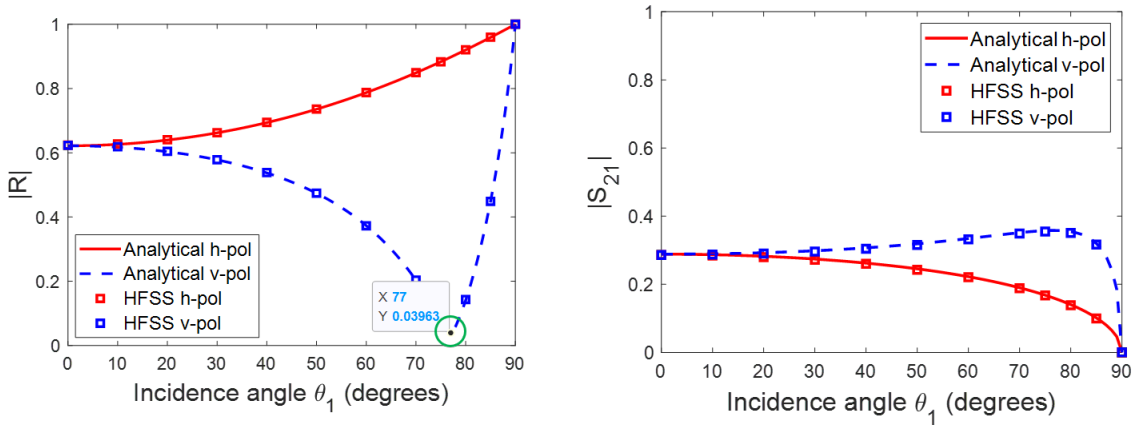

Figure 4.6 Reflection coefficient $|R|$ and transmission coefficient $|S_{21}|$ of the 0th-order Floquet mode for the case of lossy soil when the wave propagates downward.

4.1.4 Wave Propagating Upward from Soil to Air

Figure 4.7 shows that the wave propagates upward from a denser medium 1 (soil) to a less dense medium 2 (air) for each polarization. We observe how much power is reflected into soil and transmitted into air. It is noted that θ_1 is different from θ_1 used in subsection 4.1.3.

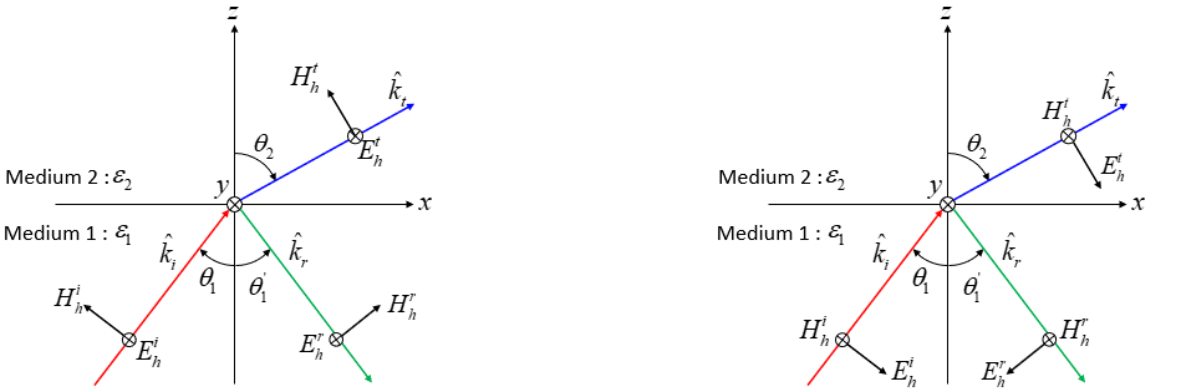

Figure 4.7 Polarized plane wave incident at an oblique incident angle on a surface where medium 1 is soil, and medium 2 is air.

4.1.4.1 Lossless Soil and Air

The 2-layer case (lossless soil and air) is modeled as shown in Figure 4.8. In the context of modeling, it is necessary to first edit the global material environment in HFSS from vacuum to soil ($\epsilon_{1r} = 18$) so that the wave propagates from inside the soil. The wavelength inside soil is 5 cm ($\lambda_0/\sqrt{\epsilon_{1r}}$). Also, differences from the model of Figure 4.2 are the unit-cell size and Floquet port location. The unit-cell size is 2.5 cm × 2.5 cm in order to make only the dominant mode become the propagation mode as mentioned in Chapter 3. The Floquet port location is switched just for the consistency such that medium 1 (soil) has port 1, medium 2 (air) has port 2.

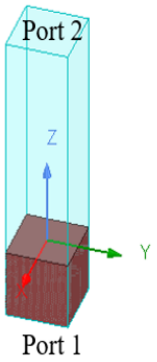

Figure 4.8 The unit cell consisting of air and soil. Radiation propagates from port 1 to port 2.

Unlike the case of the wave propagating downward, the critical angle exists. When an incidence angle is above the critical angle ($\theta_1 > \theta_c$), an evanescent wave appears, as shown in Figure 4.9, and is expressed as

$$\begin{aligned}\vec{E}^t|_{\theta_1>\theta_c} &= \hat{y}\,T^b\,E_0\,\exp(-j\beta_2 x\sin\theta_2)\exp(-j\beta_2 z\cos\theta_2)\\ &= \hat{y}\,T^b\,E_0\,\exp(-j\beta_2 x\sin\theta_2)\exp\left[-\beta_2 z\left(\sqrt{\frac{\mu_1\epsilon_1}{\mu_2\epsilon_2}\sin^2\theta_1-1}\right)\right]\\ &= \hat{y}\,T^b\,E_0\,e^{-\alpha_{2e}z}e^{-j\beta_{2e}x}\end{aligned} \tag{4.29}$$

with

$$\alpha_{2e} = \beta_2\sqrt{\frac{\mu_1\epsilon_1}{\mu_2\epsilon_2}\sin^2\theta_1-1}, \qquad \beta_{2e} = \beta_1\sin\theta_1 \tag{4.30}$$

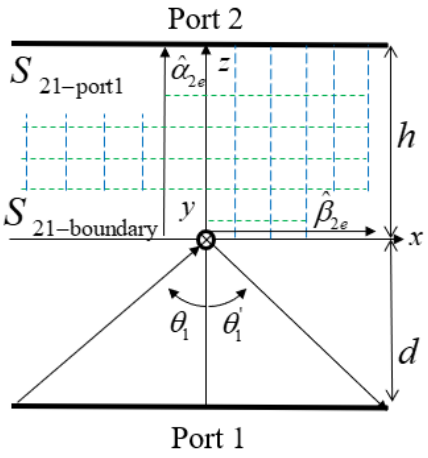

Figure 4.9 Evanescent wave propagating toward port 2 where blue and green dash lines indicate constant phase planes and amplitude planes, respectively.

where α_{2e} and β_{2e} are the effective attenuation constant and phase constant in medium 1 (air), respectively [28].

The wave associated with (4.29) propagates parallel to the boundary with constant phase planes that are parallel to the z-axis. Also, the wave decays very rapidly in the z-direction with the effective attenuation constant α_{2e}. Since the SMAP satellite is far away from the earth surface, the SMAP antenna does not consider the evanescent wave. Likewise, in the context of our modeling, we simulate the S_{21} as a function of the height of air to find the distance where the evanescent wave becomes negligible.

The analytical solutions for the $|S_{21}|^2$ at port 2 and $|S_{11}|^2$ at port 1 are computed as

$$|S_{11}|^2 = \frac{P^r}{P^i} = |R_{12}|^2 \qquad \text{for v-pol and h-pol} \tag{4.31}$$

$$\begin{aligned} |S_{21}|^2 &= e^{-2\,\alpha_{2e}h}\,\frac{\mathrm{Im}[\gamma_{2z}]}{\mathrm{Im}[\gamma_{1z}]}|T_{21}^h|^2 \qquad \text{for h-pol} \\ &= e^{-2\,\alpha_{2e}h}\,\frac{\mathrm{Im}\,[\gamma_{2z}/\epsilon_2]}{\mathrm{Im}\,[\gamma_{1z}/\epsilon_1]}|T_{21}^v|^2 \qquad \text{for v-pol} \end{aligned} \tag{4.32}$$

Figure 4.10 shows that as the height of air increases, the $|S_{21}|$ at the critical angle (13.6°) decreases, and in two wavelengths, the $|S_{21}|$ becomes negligible. Thus, we set up the height of air

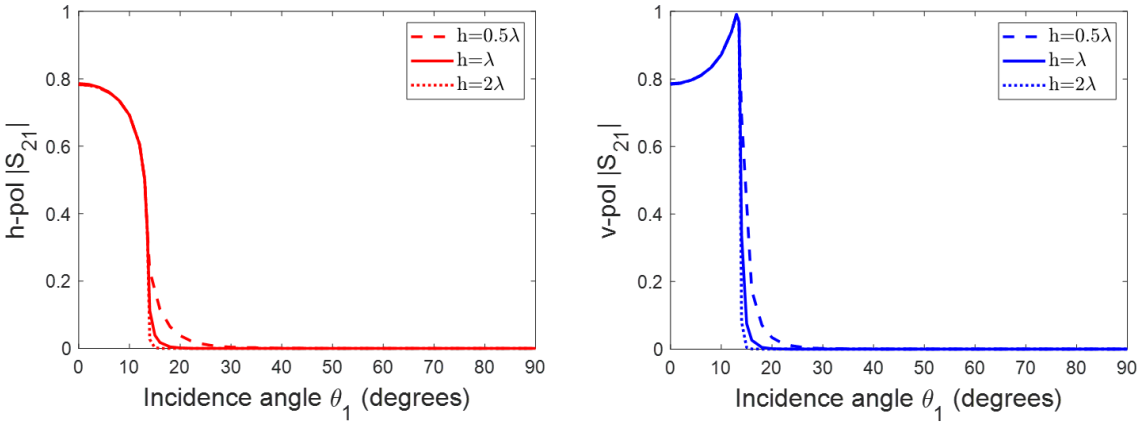

Figure 4.10 $|S_{21}|$ at port2 as a function of the air of height h in the unit cell.

in the unit cell as at least greater than two wavelengths such that port 2 does not calculate the evanescent wave.

Figure 4.11 shows that results of the two approaches are in good agreement. The Brewster angle 13.3° for the v-pol and the critical angle 13.6° for h-pol and v-pol are observed. Also, $|S_{21}|$ of v-pol is greater than that of h-pol up to the Brewster angle, and no real power is transmitted into air when the incidence angle is above the critical angle.

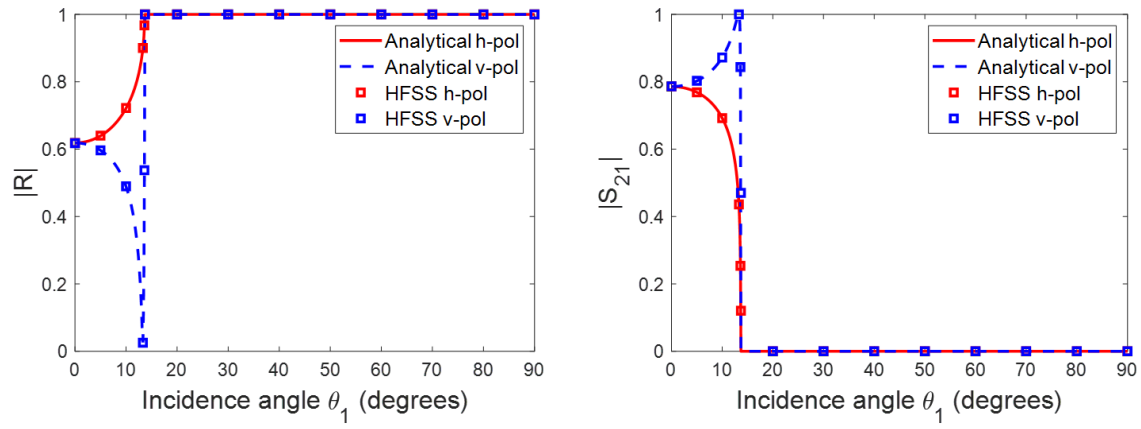

Figure 4.11 Reflection coefficient $|R|$ and transmission coefficient $|S_{21}|$ of the 0th-order Floquet mode for the case of lossless soil when the wave propagates upward.

4.1.4.2 Lossy Soil and Air

In the case of lossy soil, an deembedding formula for the analytical solution is required since the wave is attenuated with effective attenuation constants α_{1e} and α_{2e} along the z-direction as shown in Figure 4.12.

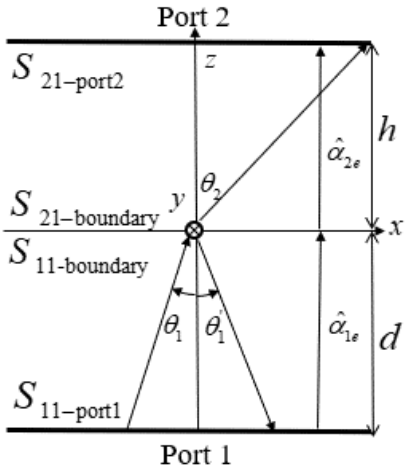

Figure 4.12 Nonuniform plane wave propagating upward from port 1 to port 2.

The reciprocity theorem is used to derive α_{1e} by assuming that the wave inside the lossy soil is a nonuniform plane wave with the constant amplitude planes parallel to the interface. The expressions of the effective attenuation constant for each medium are as follows:

For α_{1e} in medium 1 (lossy soil)

$$\alpha_{1e} = \mathrm{Re}[\gamma_{1z}] = \mathrm{Re}\left[\sqrt{\gamma_1^2 - \gamma_{1x}^2}\right] = \mathrm{Re}\left[\sqrt{\gamma_1^2 + \beta_0^2 \epsilon_{1r} \sin^2\theta_1}\right] \tag{4.33}$$

where it is noted that α_{1e} is a function of the incidence angle θ_1.

For α_{2e} in medium 2 (air)

$$\begin{aligned} \alpha_{2e} &= 0 && \text{for } \theta_1 < \theta_c \\ &= \beta_2 \ \mathrm{Re}\left[\sqrt{\left(\frac{\alpha_1 + j\beta_1}{j\beta_2}\right)^2 \sin^2\theta_1 - 1}\right] && \text{for } \theta_1 \geq \theta_c \end{aligned} \tag{4.34}$$

The analytical solutions for the $|S_{21}|^2$ at port 2 and $|S_{11}|^2$ at port 1 are computed as

$$|S_{11}|^2 = \frac{P^r}{P^i} = |R_{12}|^2\, e^{-4\,\alpha_{1e}d} \qquad \text{for v-pol and h-pol} \tag{4.35}$$

$$\begin{aligned} |S_{21}|^2 &= \frac{\mathrm{Im}[\gamma_{2z}]}{\mathrm{Im}[\gamma_{1z}]}|T_{21}^h|^2\, e^{-2\,\alpha_{1e}d}\, e^{-2\,\alpha_{2e}h} \qquad \text{for h-pol} \\ &= \frac{\mathrm{Im}\,[\gamma_{2z}/\epsilon_2]}{\mathrm{Im}\,[\gamma_{1z}/\epsilon_1]}|T_{21}^v|^2\, e^{-2\,\alpha_{1e}d}\, e^{-2\,\alpha_{2e}h} \qquad \text{for v-pol} \end{aligned} \tag{4.36}$$

The $|S_{11}|$ and $|S_{21}|$ are computed as shown in Figure 4.13. It is observed that the results of the two approaches are in good agreement. Below the critical angle (13.6°), the $|S_{21}|$ is less than that of the lossless soil case because the loss in wet soil occurs before the wave reaches the boundary. Also, there is no real power transmitted into air above the critical angle.

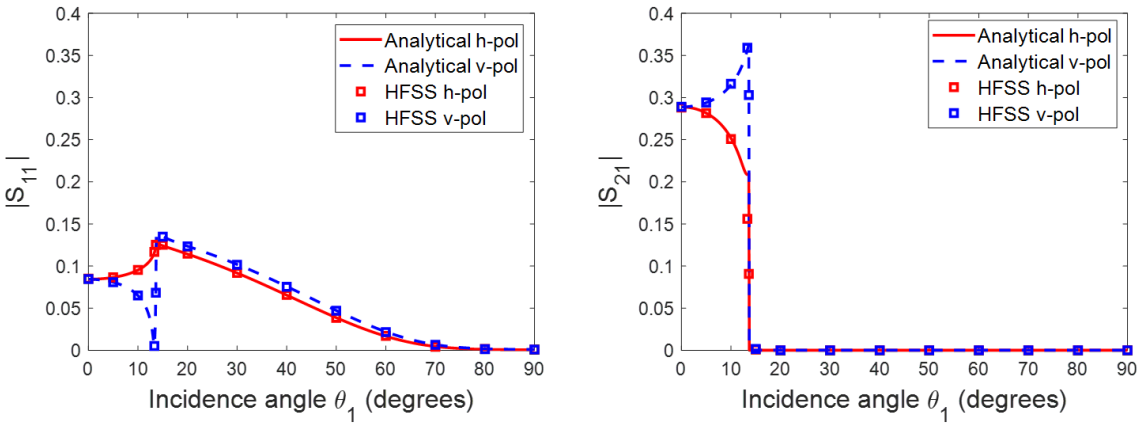

Figure 4.13 $|S_{11}|$ at port 1, and $|S_{21}|$ at port 2 of the 0th-order Floquet mode as a function of an incidence angle for the case of lossy soil.

4.2 Reflection and Transmission for 3-Layer Composite: Soil, Vegetation, and Air

As discussed in Chapter 2, the vegetation scattering effect on the brightness temperature gets significant when the plant's electrical size becomes comparable with the wavelength. In order to observe this vegetation scattering effect, we model the vegetation canopy in two different ways over the soil layer in the unit cell as shown in Figure 4.14: One model treats the vegetation canopy

as a homogeneous layer with an effective permittivity ϵ_{eff} over a soil surface. Another treats the vegetation canopy as an infinite number of finite-length cylinders that represents the plant's stem. In addition, parameters used in these two cases are shown in Table 4.1.

Figure 4.14 HFSS model: (left) vegetation canopy having effective permittivity (right) vegetation canopy consisting of infinite number of finite-length cylinders.

Table 4.1 Parameters used in 3-layer case where the operation frequency is 1.41 GHz (L-band) and the unit cell size is 10 cm×10 cm

Soil	Vegetation homogeneous layer	Vegetation stem
Depth: 9.6 cm $\epsilon_{\text{soil}} = 18 - j3$	Height: 30 cm $\epsilon_{\text{eff}} = 1.98 - j0.35$	Height: 30 cm, radius: 1.5 cm $\epsilon_{\text{stem}} = 15 - j5$

In the vegetation homogeneous layer case, th effective permittivity ϵ_{eff} is obtained by a simple dielectric mixing model where it is assumed that an equivalent dielectric constant of a heterogeneous mixture consisting of two substances (air and plant's stem) is related to the dielectric constants of the individual substances and their volume fraction. In the context of our modeling, as shown in Figure 4.14, the volume fraction of cylinder (stem) is 7.1% ($V_{\text{total}} = 3 \times 10^{-3}\,\text{m}^3$, $V_{\text{air}} = 2.788 \times 10^{-3}\,\text{m}^3$ and $V_{\text{stem}} = 2.12 \times 10^{-4}\ \text{m}^3$), and the cylinder's relative permittivity is $\epsilon_{\text{stem}} = 15 - j5$. Thus, the effective permittivity ϵ_{eff} computed by (4.37) is $1.989 - j0.353$.

$$\epsilon_{\text{eff}} = \frac{V_{\text{air}}}{V_{\text{total}}}\epsilon_{\text{air}} + \frac{V_{\text{stem}}}{V_{\text{total}}}\epsilon_{\text{stem}} \tag{4.37}$$

In the vegetation stem case, the incident wave from port 1 induces currents on cylinders, as shown in Figure 4.15, which generate the scattered radiation. As mentioned in Chapter 3, the

periodic boundary condition enforces a periodicity in the fields. Thus, $|S_{11}|$ of the vegetation stem case accounts for vegetation scattering effects such as the scattered radiation generated from the infinite number of finite-length cylinders and its coherency.

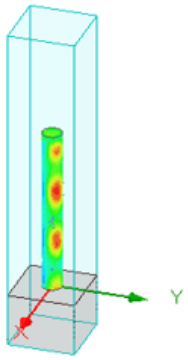

Figure 4.15 Configuration of induced current on cylinder.

4.2.1 Wave Propagating Downward from Air to Soil through Vegetation Canopy

The case where wave propagates downward from port 1 (air) to port 2 (soil) is simulated, and we observe how much power is reflected into air for different two cases. In order to validate our model with an analytical solution, the total reflection coefficient by 3-layers medium with known constitutive parameters is computed. The details for the derivation are given in Appendix C.

$$R^{\text{total}} = \frac{R_{12} + R_{23}\, e^{-2\gamma_{2z}h}}{1 + R_{12}R_{23}\, e^{-2\gamma_{2z}h}} \tag{4.38}$$

where R^{total} is equal to the sum of all of wave propagating upward in medium 1 (air); R_{12} and R_{23} are the reflection coefficients at each boundary, like from an interface between two half spaces, which can be obtained by the same method of (4.6) and (4.9); h is the vegetation canopy's height as shown in Figure 4.16.

Figure 4.17 shows that first, the results of the two approaches (analytical solution and homogeneous layer case) are in good agreement, and the reflection of the incident wave from the multilayered medium can be derived using the HFSS unit cell technique. Second, replacing vegetation canopy with the homogeneous layer using effective permittivity based on the volume fraction

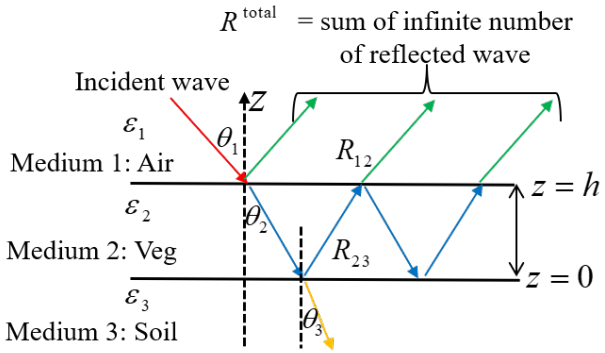

Figure 4.16 Multiple reflections in a 3-layer composite.

of air to stem is not adequate. It is because that this approach does not account for the vegetation scattered radiation and its coherency. Also, the cylinder's electrical size compared to the wavelength (21 cm) is not small enough, such that multiple scattering from the cylinders can not be negligible. Third, the $|S_{11}|$ of the stem case is greater than that of the homogeneous layer case for most angles. More results as a function of the vegetation canopy's height are shown in Figure 4.18 and Figure 4.19.

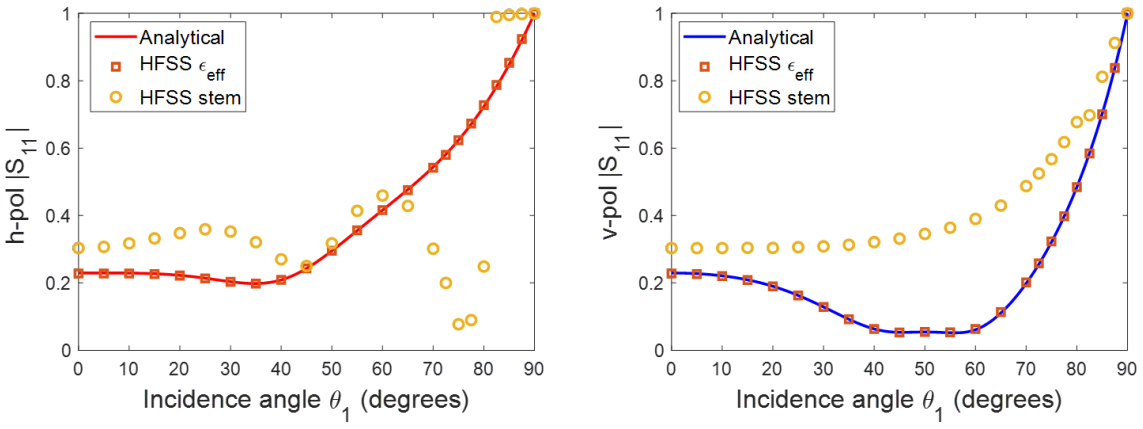

Figure 4.17 $|S_{11}|$ of three different approaches; analytical solution, HFSS model with the vegetation homogeneous layer and HFSS model with the vegetation stem when the vegetation canopy's height is 30 cm.

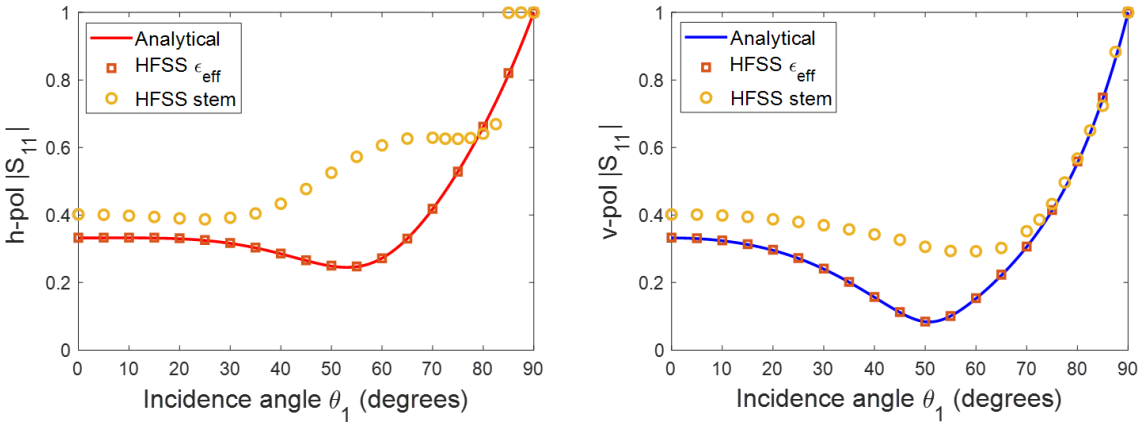

Figure 4.18 $|S_{11}|$ when the vegetation canopy's height is 15 cm.

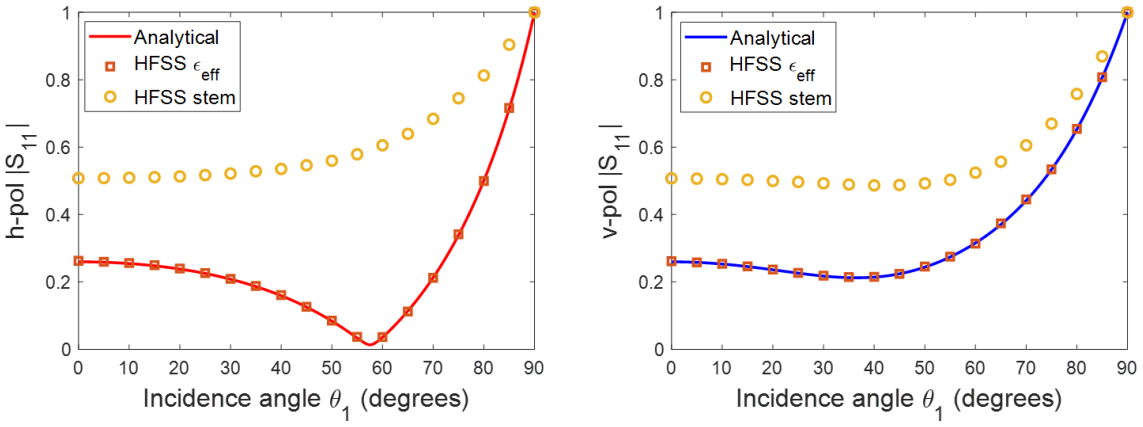

Figure 4.19 $|S_{11}|$ when the vegetation canopy's height is 5 cm.

4.2.2 Wave Propagating Upward from Soil to Air through Vegetation Canopy

The case where wave propagates upward from port 1 (soil) to port 2 (air) is simulated, and then transmission coefficient S_{21} is derived as a function of different vegetation heights; 1 cm, 20 cm, 30 cm. The S_{21} indicates how much power of v- or h-polarized radiation is transmitted into air.

We first validate the accuracy of S_{21} of the homogeneous layer case by comparing it with an analytical solution. The derivation of total transmission coefficient is illustrated in [28].

$$T^{\text{total}} = \frac{T_{32}T_{21}}{1 - R_{21}R_{23}\, e^{-2\gamma_{2z}h}} \tag{4.39}$$

where T^{total} is overall transmission coefficient in medium 3 (air); T_{32}, T_{21}, R_{21}, and R_{23} are the reflection and transmission coefficients at each boundary, like from an interface between two half spaces, which can be obtained by the same method of (4.6), (4.7), (4.9), and (4.10); h is the vegetation canopy's height; d is the soil depth; α_{1e} and α_{2e} are the effective attenuation constants as shown in Figure 4.20.

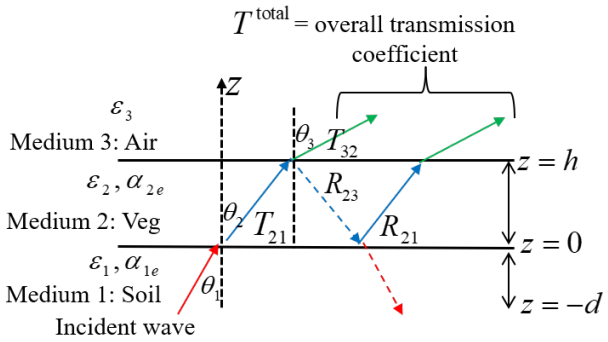

Figure 4.20 Multiple transmission in a 3-layer composite.

The analytical solution for the $|S_{21}|^2$ at port 2 of the vegetation homogeneous layer case are computed as

$$\begin{aligned} |S_{21}|^2 &= \frac{\text{Im}[\gamma_{3z}]}{\text{Im}[\gamma_{1z}]}|T_h^{\text{total}}|^2\, e^{-2\,\alpha_{1e}d}\, e^{-2\,\alpha_{2e}h} \qquad \text{for h-pol} \\ &= \frac{\text{Im}\,[\gamma_{3z}/\epsilon_3]}{\text{Im}\,[\gamma_{1z}/\epsilon_1]}|T_v^{\text{total}}|^2\, e^{-2\,\alpha_{1e}d}\, e^{-2\,\alpha_{2e}h} \qquad \text{for v-pol} \end{aligned} \tag{4.40}$$

Figure 4.21 shows that the results of the two approaches (analytical solution and homogeneous layer case) are in good agreement.

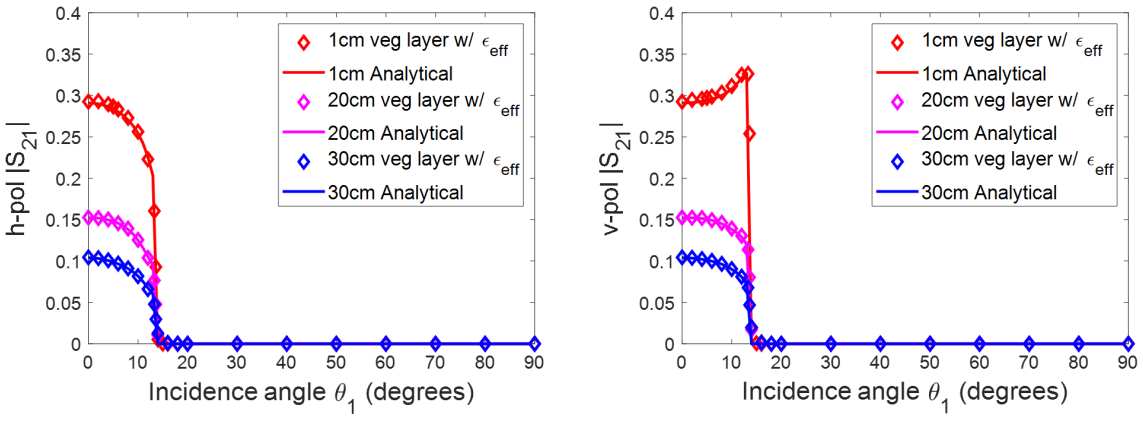

Figure 4.21 Comparison an analytical solution with a homogeneous layer with an effective permittivity case as a function of different heights of the vegetation canopy.

Figure 4.22 shows that first, the effect of vegetation canopy with 1 cm height on the observed brightness temperature is small because the results of vegetation canopy with 1 cm height are almost the same as that of a 2-layer case. It does physically make sense because 1 cm is much smaller compared to the observation's wavelength of 21 cm. In other words, the SMAP satellite can see the soil surface clearly when the vegetation canopy's height is 1 cm. Second, $|S_{21}|$ of v-pol is greater than that of h-pol up to Brewster angle around 15°, but when the vegetation canopy gets thicker, both $|S_{21}|$ of h-pol and v-pol decreases continuously as the incidence angle increases. Third, $|S_{21}|$ gets smaller as the vegetation canopy gets thicker because more loss occurs when the traveling path within the vegetation canopy gets longer. Fourth, $|S_{21}|$ of the stem case is greater than that of the homogeneous layer case, and the difference between the two cases become larger when the vegetation canopy's height increases. Thus, it is concluded that the vegetation scattering effect cannot be negligible as plants grow taller.

4.3 Transmissivity and Frequency-Selective Response of Vegetation Canopy

The vegetation canopy itself without the soil layer is simulated to derive the transmissivity that is directly related to the vegetation optical depth. Furthermore, the accuracy of our method is validated by comparing with the literature [2].

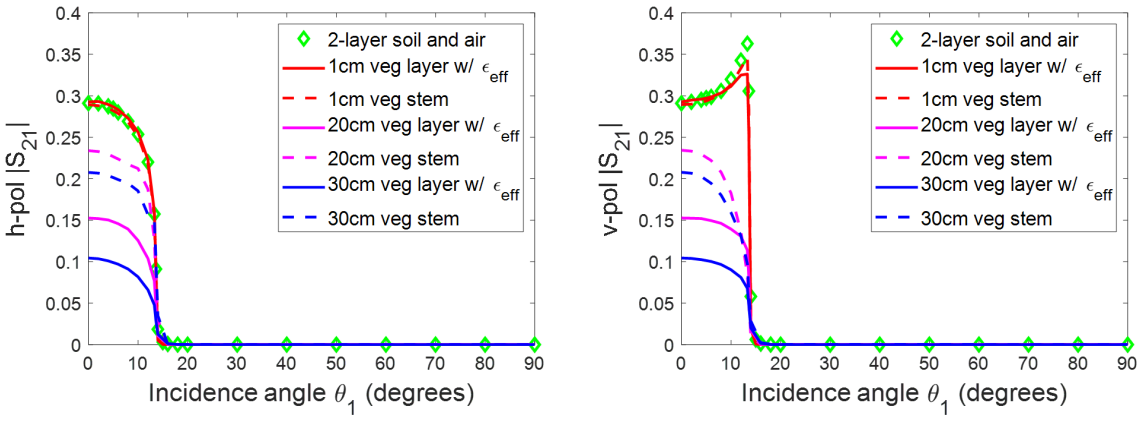

Figure 4.22 $|S_{21}|$ at port 2 as a function of different vegetation heights for three different approaches; HFSS model with 2-layer case, HFSS model with the effective permittivity, and HFSS model with the stem.

In Figure 4.23, the sparsely distributed case is for the literature, and the periodically distributed case is for our model. Parameters used in these two cases are as follows: the cylinder has the radius of 1 mm, length of 30 cm, and relative complex permittivity of $30.7 - j5.5$; the operation frequency is 5.4 GHz (C-band), and the wavelength is 5.5 cm; the density is 2122 number of cylinders per m^2; the incident angle is 40°. Those parameters represent the water column density 1 $kg{\cdot}m^{-2}$ of the grass canopy.

In addition, the same density of grass canopy must be used in the context of modeling the grass canopy in order to compare with the literature. As shown in Figure 4.24, cylinders are distributed with the same spacing, and the spacing is derived by following procedure. Each row in the square of 1 m^2 has n-cylinders. This yields

$$n^2 = 2122, \qquad (n-1)s + 2r = 1 \tag{4.41}$$

where s is the spacing between cylinders, and r is the radius of cylinder. The (4.41) results in the spacing 2.17 cm with which the periodically distributed case of the grass canopy is modeled as shown in Figure 4.25.

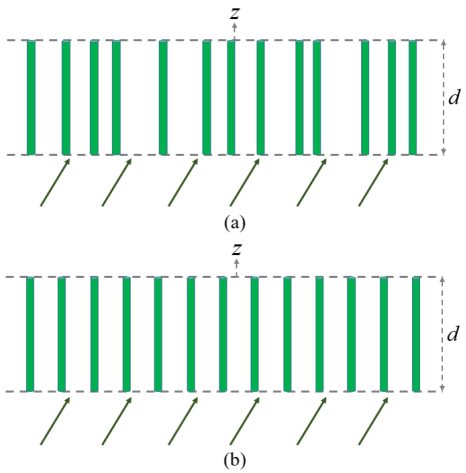

Figure 4.23 One layer consisting of long and thin cylinders (a) sparsely distributed [2] (b) periodically distributed with the spacing between cylinders of 2.17 cm.

The transmissivity γ is computed using S-parameters as follow:

$$\gamma = \frac{P^t}{P^i} = \frac{|S_{(1,\mathrm{h})(2,\mathrm{h})}|^2 + |S_{(1,\mathrm{h})(2,\mathrm{v})}|^2 + |S_{(1,\mathrm{v})(2,\mathrm{h})}|^2 + |S_{(1,\mathrm{v})(2,\mathrm{v})}|^2}{2} \tag{4.42}$$

where P^t and P^i are the transmitted and incident powers, respectively, the subscripts 1 and 2 denote each port, the subscripts h and v indicate the polarization, and denominator 2 is the total excitation power from port 2. In detail, we assign the same power of 1 W to each TE_{00} and TM_{00} Floquet mode, as shown in Figure 4.26, in order to excite the unpolarized radiation from port 2. Again, the unpolarized radiation is the radiation when the magnitudes of h-pol and v-pol are the same.

Transmissivity in Table 4.2 is computed by (4.42). It is observed that as the incident angle increases, transmissivity decreases. It physically makes sense that the energy loss becomes larger as the path on which the wave travels through the vegetation canopy gets longer. 0.7768 at 40° is noticeable because 40° is the incidence angle of the literature and the SMAP satellite.

Table 4.2 Transmissivity as a function of an incident angle

Incident angle [deg]	0	20	30	**40**	50	60	70	90
Transmissivity	0.9890	0.9339	0.8659	**0.7768**	0.6802	0.5956	0.5363	0

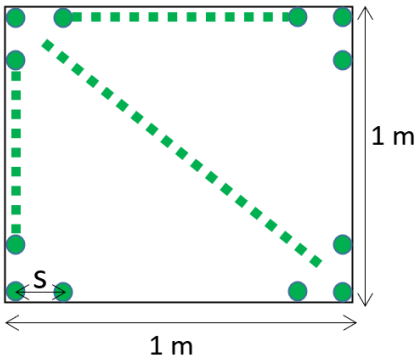

Figure 4.24 Top view of the periodically distributed case with the density of 2122 number of cylinders per m^2 where s denotes the spacing between cylinders.

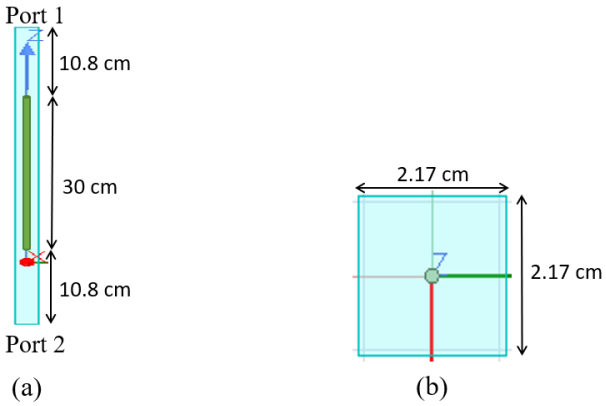

Figure 4.25 HFSS modeling for the grass canopy with the dimension of unit cell and cylinder (a) front view (b) top view.

It is necessary to illustrate the concept of two methods introduced in [2] before comparing with our results. The VRT (vector radiative transfer) [29] is a radar scattering model for the vegetation canopy which is treated as a homogeneous layer with an effective permittivity like the $\tau - \omega$ model. In this method, the extinction coefficient κ_e is numerically calculated by (2.11). Using (2.12), the transmissivity can be calculated based on κ_e. The NMM3D (numerical Maxwell model in 3D simulations) [2] is the full wave approach for solving the Maxwell equation directly such that the calculation of κ_e is not needed, and the scattered radiation and its coherency are considered.

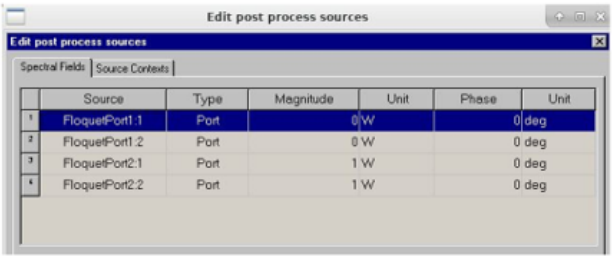

Figure 4.26 Assigning the power on source in HFSS where FloquetPort 2:1 and FloquetPort 2:2 are TE_{00} and TM_{00} Floquet mode respectively at port 2.

Table 4.3 Transmissivity at an incident angle 40°, showing difference between the proposed approach using the HFSS and the literature results for the clustered case using NMM3D and VRT [2]. $e^{-\tau/\cos\theta} = \gamma \Rightarrow \tau = -\cos\theta \ln\gamma$

Grass Canopy (Vegetation Water Content 1 kg·m^{-2})			
Methodology / Distribution	HFSS / Periodically	NMM3D / Sparsely	VRT / Sparsely
Transmissivity (γ)	0.7768	0.7044	0.1722
VOD (τ)	0.6449	0.8948	4.4918

Table 4.3 shows the comparison between our result and the literature for the case of Figure 4.23. First, values of transmissivity derived by two methods (NMM3D and VRT) are compared each other in [2]. Then, it is concluded that VRT overestimates an attenuation through the vegetation canopy since transmissivity of 0.7044 in NMM3D is much greater than that of 0.1722 in VRT. Second, it is observed that the transmissivity of 0.7768 in our proposed approach (HFSS model) is slightly greater than that of 0.7044 in NMM3D. It can be assumed that more coherent wave interactions take place among the vegetation scatters in the periodically distributed case than in the sparsely distributed case. Third, since 0.7044 of the NMM3D is an average value of transmissivity with having the standard deviation 0.201, the transmissivity 0.7768 of HFSS model is in the range of the NMM3D with the sparsely distributed case. Fourth, the transmissivity values of our proposed approach and the NMM3D are much greater than that of VRT. In other words, the VOD of the HFSS and NMM3D is much lower than that of VRT. It is because the HFSS model and NMM3D account for the scattered radiation and its coherency by solving Maxwell equation directly.

Besides, we can derive the transmissivity as a function of frequency as shown in Figure 4.27. It shows that as frequency increases, the transmissivity decreases. In other words, grass vegetation canopy is getting opaque as the wavelength becomes shorter. Also, Table 4.4 shows that the vertically polarized loss is greater than the horizontally polarized loss since the vegetation canopy consists of vertically oriented stems.

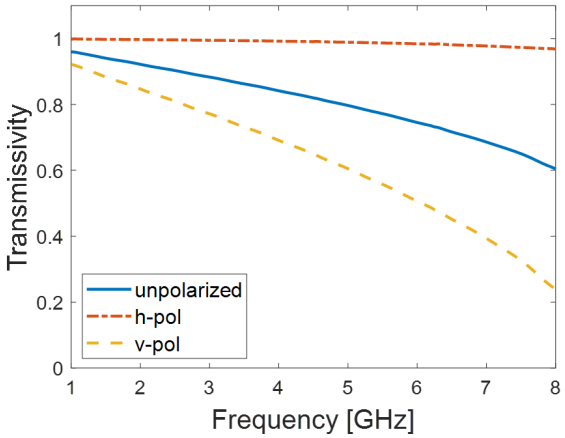

Figure 4.27 Grass canopy transmissivity for each polarization as a function of frequency (f: 1 - 8 GHz, λ: 7.5 cm - 3.75 cm).

Table 4.4 Grass canopy transmissivity for each polarization

Transmissivity		
Frequency	**1.41 GHz (L-band)**	**5.4 GHz (C-band)**
Unpolarized	0.9443	0.7768
H-pol	0.9978	0.9870
V-pol	0.8907	0.5657

CHAPTER 5. CONCLUSIONS

In this thesis, the vegetation scattering effect is studied as a part of an effort to reduce the SMAP product's seasonal bias in cropland. In the context of the SMAP performance using L-band, the $\tau - \omega$ model treats the vegetation scattering as almost zero. However, our simulation results show that when the electrical size of plants becomes larger enough to be comparable with the observation wavelength, the vegetation scattering effect can not be negligible.

Our proposed approach uses the Floquet port and periodic boundary condition in HFSS. In this manner, we model the vegetation canopy consisting of an infinite number of finite-length cylinders and excited the unpolarized plane wave (v-pol and h-pol) with oblique incidence from the port. S-parameters of the zeroth-order Floquet mode (TE_{00} mode and TM_{00} mode) were utilized in order to get the reflection and transmission coefficients and transmissivity of the vegetation canopy.

For the two-layer case (soil and air), we derive the reflection and transmission coefficients at the boundary between bare soil and air both and validate our model by comparing with the analytical solution. For the three-layer case (soil, vegetation canopy, and air), it shows that treating the vegetation canopy as the homogeneous layer with effective permittivity based on only the volume fraction is found not to be adequate in the way of representing the vegetation canopy. Also, we observe that the vegetation scattering effect becomes larger as plants grow taller. For the vegetation canopy itself without soil layer, the transmissivity of grass canopy that is directly related to the vegetation optical depth is calculated as a function of the incident angle as well as the frequency. Our proposed approach is validated by comparing with the literature.

In conclusion, we show the vegetation scattering effect and derive the vegetation optical depth for grass canopy through our proposed approach where the scattered fields and coherent wave interactions are considered by solving the Maxwell equation directly. In the later study, the corn canopy will be modeled by adjusting the unit-cell size and using the realistic 3D model of corn, and

the simulation results will be compared with the literature where the transmissivity of a vegetation canopy is measured experimentally.

BIBLIOGRAPHY

[1] V. A. Walker, B. K. Hornbuckle, M. H. Cosh, and J. H. Prueger, "Seasonal evaluation of SMAP soil moisture in the U.S. corn belt," *Remote Sensing*, vol. 11, no. 21, 2019. [Online]. Available: https://www.mdpi.com/2072-4292/11/21/2488

[2] H. Huang, L. Tsang, E. G. Njoku, and A. Colliander, "A new vegetation model based on numerical 3D solutions of Maxwell equations," in *2017 IEEE International Geoscience and Remote Sensing Symposium (IGARSS)*, July 2017, pp. 2903–2906.

[3] M. Spencer, S. Chan, L. Veilleux, and K. Wheeler, "The soil moisture active/passive (SMAP) mission radar: A novel conically scanning SAR," in *2009 IEEE Radar Conference*, May 2009, pp. 1–4.

[4] F. T. Ulaby, P. C. Dubois, and J. van Zyl, "Radar mapping of surface soil moisture," *Journal of Hydrology*, vol. 184, no. 1, pp. 57–84, 1996, soil Moisture Theories and Observations. [Online]. Available: http://www.sciencedirect.com/science/article/pii/0022169495029680

[5] P. O'Neill, S. Chan, E. Njoku, T. Jackson, and R. Bindlish, "Algorithm theoretical basis document level 2 & 3 soil moisture (passive) data products; revision B," *Jet Propulsion Lab., California Inst. Technol.: Pasadena, CA, USA*, 2017.

[6] S. K. Chan, R. Bindlish, P. E. O'Neill, E. Njoku, T. Jackson, A. Colliander, F. Chen, M. Burgin, S. Dunbar, J. Piepmeier, S. Yueh, D. Entekhabi, M. H. Cosh, T. Caldwell, J. Walker, X. Wu, A. Berg, T. Rowlandson, A. Pacheco, H. McNairn, M. Thibeault, J. Martínez-Fernández, González-Zamora, M. Seyfried, D. Bosch, P. Starks, D. Goodrich, J. Prueger, M. Palecki, E. E. Small, M. Zreda, J. Calvet, W. T. Crow, and Y. Kerr, "Assessment of the SMAP passive soil moisture product," *IEEE Transactions on Geoscience and Remote Sensing*, vol. 54, no. 8, pp. 4994–5007, Aug 2016.

[7] I. Mladenova, T. Jackson, E. Njoku, R. Bindlish, S. Chan, M. Cosh, T. Holmes, R. de Jeu, L. Jones, J. Kimball, S. Paloscia, and E. Santi, "Remote monitoring of soil moisture using passive microwave-based techniques — theoretical basis and overview of selected algorithms for AMSR-E," *Remote Sensing of Environment*, vol. 144, pp. 197–213, 2014. [Online]. Available: http://www.sciencedirect.com/science/article/pii/S0034425714000261

[8] S. N. Makarov and A. Puzella, "Scan impedance for an infinite dipole array: Hansen's formulas compared with ansoft HFSS simulations [EM programmer's notebook]," *IEEE Antennas and Propagation Magazine*, vol. 49, no. 4, pp. 143–156, Aug 2007.

[9] M. N. Hasan, *Floquet Theory and Mathematical Approach to Unit Cell Analysis*, Tensorbundle Lab, 2019, Accessed: 2020-04-20. [Online]. Available: https://tensorbundle.wixsite.com/home

[10] A. K. Bhattacharyya, *Phased Array Antennas: Floquet Analysis, Synthesis, BFNs and Active Array Systems*, 1st ed. Wiley-Interscience, 2006.

[11] S. Chan, R. Bindlish, P. O'Neill, T. Jackson, E. Njoku, S. Dunbar, J. Chaubell, J. Piepmeier, S. Yueh, D. Entekhabi, A. Colliander, F. Chen, M. Cosh, T. Caldwell, J. Walker, A. Berg, H. McNairn, M. Thibeault, J. Martínez-Fernández, F. Uldall, M. Seyfried, D. Bosch, P. Starks, C. H. Collins, J. Prueger, R. van der Velde, J. Asanuma, M. Palecki, E. Small, M. Zreda, J. Calvet, W. Crow, and Y. Kerr, "Development and assessment of the SMAP enhanced passive soil moisture product," *Remote Sensing of Environment*, vol. 204, pp. 931–941, 2018. [Online]. Available: http://www.sciencedirect.com/science/article/pii/S0034425717303917

[12] V. A. Walker, "A new approach for retrieving soil moisture from SMAP over the corn belt," Ph.D. dissertation, Iowa State University, Ames, Iowa, USA, 2019.

[13] J. Patton and B. Hornbuckle, "Initial validation of SMOS vegetation optical thickness in iowa," *IEEE Geoscience and Remote Sensing Letters*, vol. 10, no. 4, pp. 647–651, July 2013.

[14] M. Kurum, "Quantifying scattering albedo in microwave emission of vegetated terrain," *Remote Sensing of Environment*, vol. 129, pp. 66–74, 2013. [Online]. Available: http://www.sciencedirect.com/science/article/pii/S0034425712004099

[15] B. K. Hornbuckle, A. W. England, R. D. De Roo, M. A. Fischman, and D. L. Boprie, "Vegetation canopy anisotropy at 1.4 GHz," *IEEE Transactions on Geoscience and Remote Sensing*, vol. 41, no. 10, pp. 2211–2223, Oct 2003.

[16] B. K. Hornbuckle and A. W. England, "Radiometric sensitivity to soil moisture at 1.4 GHz through a corn crop at maximum biomass," *Water Resources Research*, vol. 40, no. 10, 2004. [Online]. Available: https://agupubs.onlinelibrary.wiley.com/doi/abs/10.1029/2003WR002931

[17] B. K. Hornbuckle and T. L. Rowlandson, "Evaluating the first-order tau-omega model of terrestrial microwave emission," in *IGARSS 2008 - 2008 IEEE International Geoscience and Remote Sensing Symposium*, vol. 1, July 2008, pp. I–193–I–196.

[18] ANSYS, "HFSS workshop 9-1: Unit cell analysis (infinite array)," Canonsburg, PA, USA, 2015. [Online]. Available: http://www.ece.uprm.edu/~rafaelr/inel6068/HFSS/HFSS_Antenna_v2015_v1/workshop_instructions_trainee/ANSYS_HFSS_Antenna_W09_1_Unit_Cell.pdf

[19] F. T. Ulaby and D. G. Long, *Microwave Radar and Radiometric Remote Sensing*, ser. Microwave Radar and Radiometric Remote Sensing. The University of Michigan Press, 2014, vol. 1.

[20] T. Mo, B. J. Choudhury, T. J. Schmugge, J. R. Wang, and T. J. Jackson, "A model for microwave emission from vegetation-covered fields," *Journal of Geophysical*

Research: Oceans, vol. 87, no. C13, pp. 11 229–11 237, 1982. [Online]. Available: https://agupubs.onlinelibrary.wiley.com/doi/abs/10.1029/JC087iC13p11229

[21] J.-P. Wigneron, T. Jackson, P. O'Neill, G. D. Lannoy, P. de Rosnay, J. Walker, P. Ferrazzoli, V. Mironov, S. Bircher, J. Grant, M. Kurum, M. Schwank, J. Munoz-Sabater, N. Das, A. Royer, A. Al-Yaari, A. A. Bitar, R. Fernandez-Moran, H. Lawrence, A. Mialon, M. Parrens, P. Richaume, S. Delwart, and Y. Kerr, "Modelling the passive microwave signature from land surfaces: A review of recent results and application to the L-band SMOS & SMAP soil moisture retrieval algorithms," *Remote Sensing of Environment*, vol. 192, pp. 238–262, 2017. [Online]. Available: http://www.sciencedirect.com/science/article/pii/S0034425717300366

[22] J.-P. Wigneron, M. Parde, P. Waldteufel, A. Chanzy, Y. Kerr, S. Schmidl, and N. Skou, "Characterizing the dependence of vegetation model parameters on crop structure, incidence angle, and polarization at L-band," *IEEE Transactions on Geoscience and Remote Sensing*, vol. 42, no. 2, pp. 416–425, 2004.

[23] T. Jackson and T. Schmugge, "Vegetation effects on the microwave emission of soils," *Remote Sensing of Environment*, vol. 36, no. 3, pp. 203–212, 1991. [Online]. Available: http://www.sciencedirect.com/science/article/pii/003442579190057D

[24] B. J. Choudhury, T. J. Schmugge, A. Chang, and R. W. Newton, "Effect of surface roughness on the microwave emission from soils," *Journal of Geophysical Research: Oceans*, vol. 84, no. C9, pp. 5699–5706, 1979. [Online]. Available: https://agupubs.onlinelibrary.wiley.com/doi/abs/10.1029/JC084iC09p05699

[25] J. R. Wang and T. J. Schmugge, "An empirical model for the complex dielectric permittivity of soils as a function of water content," *IEEE Transactions on Geoscience and Remote Sensing*, vol. 18, no. 4, pp. 288–295, Oct 1980.

[26] F. G. Hu, "Integral equation analysis of electromagnetic wave propagation in periodic structure and error analysis of various basis functions in projection of plane waves," Ph.D. dissertation, Iowa State University, Ames, Iowa, USA, 2010.

[27] M. C. Dobson, F. T. Ulaby, M. T. Hallikainen, and M. A. El-rayes, "Microwave dielectric behavior of wet soil-part II: Dielectric mixing models," *IEEE Transactions on Geoscience and Remote Sensing*, vol. 23, no. 1, pp. 35–46, Jan 1985.

[28] C. A. Balanis, *Advanced engineering electromagnetics*, 2nd ed. John Wiley & Sons, 2012.

[29] F. T. Ulaby, K. Sarabandi, K. Mcdonald, M. Whitt, and M. C. Dobson, "Michigan microwave canopy scattering model," *International Journal of Remote Sensing*, vol. 11, no. 7, pp. 1223–1253, 1990. [Online]. Available: https://doi.org/10.1080/01431169008955090

APPENDIX A. PROOF OF IDENTIFYING THE INFINITE SERIES OF EXPONENTIAL FUNCTIONS TO INFINITE SERIES OF DIRAC DELTA FUNCTIONS

Formulations for the proof follow [10]. A periodic function $h(x)$ of periodicity b can be expressed in terms of a Fourier series as

$$h(x) = \sum_{m=-\infty}^{+\infty} A_m \exp(\frac{j2mx\pi}{b}) \tag{A.1}$$

The unknown coefficient A_m can be derived multiplying both sides by $\exp(-j2nx\pi/b)$ and then integrating in a full period of $h(x)$. This yields

$$A_m = \frac{1}{b}\int_{-b/2}^{b/2} h(x)\exp(\frac{-j2mx\pi}{b})dx \quad m = 0, \pm1, \pm2, \cdots \tag{A.2}$$

For infinite series of Dirac delta functions, $h(x) = \sum_{m=-\infty}^{\infty}\delta(x-ma)$. Thus for $-b/2 < x < b/2$, $h(x) = \delta(x)$. Using this in (A.2), we obtain

$$A_m = \frac{1}{b}\int_{-b/2}^{b/2} \delta(x)\exp(\frac{-j2mx\pi}{b})dx = \frac{1}{b} \tag{A.3}$$

Substituting A_m of (A.3) into (A.1), we have

$$\sum_{m=-\infty}^{\infty}\delta(x-mb) = \frac{1}{b}\sum_{m=-\infty}^{\infty}\exp(\frac{j2mx\pi}{b}) \tag{A.4}$$

The alternative form is obtained by replacing x by $k_x - k_0$ and b by $2\pi/a$ in (A.4). This yields

$$\frac{2\pi}{a}\sum_{m=-\infty}^{\infty}\delta(k_x - k_0 - \frac{2m\pi}{a}) = \sum_{m=-\infty}^{\infty}\exp\{jma(k_x - k_0)\} \tag{A.5}$$

APPENDIX B. RELATIONSHIP BETWEEN PROPAGATING FLOQUET MODES AND UNIT-CELL SIZE

The formulations in this section follow [10]. For a rectangular grid as discussed in Chapter 3, we derive the Floquet modes as follows:

$$k_{xmn} = k_{x0} + \frac{2m\pi}{a} \qquad k_{ymn} = k_{y0} + \frac{2n\pi}{b} \tag{B.1}$$

Also, the dominant Floquet mode is expressed as

$$k_{x0} = k_0 \sin\theta_0 \cos\phi_0 \tag{B.2a}$$

$$k_{y0} = k_0 \sin\theta_0 \sin\phi_0 \tag{B.2b}$$

Combining (B.1) and (B.2) we derive for the (m, n) Floquet mode

$$\left(k_{xmn} - \frac{2m\pi}{a}\right)^2 + \left(k_{ymn} - \frac{2n\pi}{b}\right)^2 = k_0^2 \sin^2\theta_0 \leq k_0^2 \tag{B.3}$$

(B.3) represents sets of circular regions of radius k_0 as shown in Figure B.1.

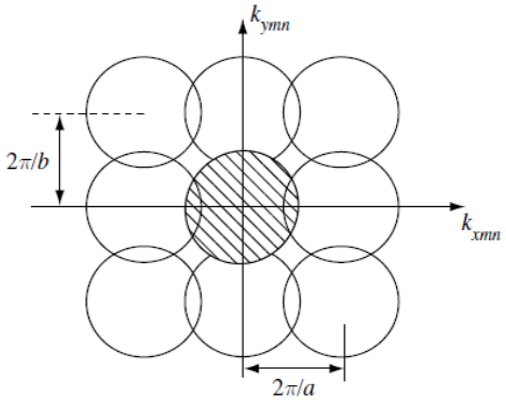

Figure B.1 Circle diagram for rectangular grid [10].

Each circle with the radius k_0 represents a Floquet Mode, and the circle located at the origin indicates the dominant Floquet mode with $m = n = 0$. It is observed that if k_0 follows a condition

(B.4), all the mode circles except the dominant mode circle do not intersect the shaded region. Also, the Floquet modes associated with such circles become the evanescent modes because all the points inside such circles do not satisfy (B.3).

$$k_0 < \frac{\pi}{a}, \qquad k_0 < \frac{\pi}{b} \tag{B.4}$$

Substituting $k_0 = 2\pi/\lambda_0$ into (B.4), this yields

$$a < \frac{\lambda_0}{2}, \qquad b < \frac{\lambda_0}{2} \tag{B.5}$$

Thus, if the unit-cell sizes a and b do not exceed $\lambda_0/2$, there is only the dominant mode propagating in the unit cell, and other modes experience attenuation and decay in z-direction.

APPENDIX C. TOTAL REFLECTION COEFFICIENT FOR 3-LAYER COMPOSITE

The formulations in this section follow [19]. our model has three-layer composite; medium 1 (air), medium 2 (vegetation canopy layer of thickness d), and medium 3 (soil). These three media are characterized by constitutive parameters as follows:

for medium 1 air: ϵ_0, μ_0, and $\sigma_1 = 0$

$$\alpha_1 = 0, \qquad \gamma_1 = jk_1 \qquad \eta_1 = \eta_0 \tag{C.1}$$

for medium 2 vegetation canopy layer: $\epsilon_2 = \epsilon_2' - j\epsilon_2''$ and μ_0

$$\gamma_2 = \alpha_2 + j\beta_2 = k_0\sqrt{-\epsilon_2} \qquad \eta_2 = \frac{\eta_0}{\sqrt{\epsilon_2}} \tag{C.2}$$

for medium 3 soil: $\epsilon_3 = \epsilon_3' - j\epsilon_3''$ and μ_0

$$\gamma_3 = \alpha_3 + j\beta_3 = k_0\sqrt{-\epsilon_3} \qquad \eta_3 = \frac{\eta_0}{\sqrt{\epsilon_3}} \tag{C.3}$$

Under the Snell's law phase-matching condition

$$\gamma_1 \sin\theta_1 = \gamma_2 \sin\theta_2 = \gamma_3 \sin\theta_3 \tag{C.4a}$$

$$\cos\theta_2 = \sqrt{1 - \left(\frac{\gamma_1}{\gamma_2}\sin\theta_1\right)^2} \tag{C.4b}$$

$$\cos\theta_3 = \sqrt{1 - \left(\frac{\gamma_1}{\gamma_3}\sin\theta_1\right)^2} \tag{C.4c}$$

As shown in Figure 4.16, we assume that the incident electric field is expressed as

$$\mathbf{E}_1^- = \hat{y}A_1 e^{-jk_1(x\sin\theta_1 - z\cos\theta_1)} \tag{C.5}$$

where A_1 is the amplitude of $\mathbf{E}_1^-$ at $x = 0$ and $z = 0$, $\mathbf{E}_1^-$ denotes that electric field in medium 1 propagates downward. Similarly, the electric field propagating upward in medium 1 is expressed as

$$\mathbf{E}_1^+ = \hat{y}B_1 e^{-jk_1(x\sin\theta_1 + z\cos\theta_1)} \tag{C.6}$$

where B_1 is the amplitude of the sum of the electric fields that are multiple-reflected back into medium 1, $\mathbf{E}_1^+$ denotes that electric field in medium 1 propagates upward. Thus, total electric field in medium 1 is

$$\mathbf{E}_1 = \mathbf{E}_1^- + \mathbf{E}_1^+ = \hat{y}(A_1 e^{jk_1 z\cos\theta_1} + B_1 e^{-jk_1 z\cos\theta_1})e^{-jk_1 x\sin\theta_1} \tag{C.7}$$

Similarly, total magnetic field in medium 1 is

$$\mathbf{H}_1 = \hat{x}H_{1x} + \hat{z}H_{1z} \tag{C.8}$$

with

$$H_{1x} = \frac{\cos\theta_1}{\eta_1}(A_1 e^{jk_1 z\cos\theta_1} - B_1 e^{-jk_1 z\cos\theta_1})e^{-jk_1 x\sin\theta_1} \tag{C.9a}$$

$$H_{1z} = \frac{\sin\theta_1}{\eta_1}(A_1 e^{jk_1 z\cos\theta_1} + B_1 e^{-jk_1 z\cos\theta_1})e^{-jk_1 x\sin\theta_1} \tag{C.9b}$$

The x component of the phase in all of expressions for fields in different medium are identical by Snell's law. Then the phase matching condition are given by

$$e^{-jk_1 x\sin\theta_1} = e^{-\gamma_2 x\sin\theta_2} = e^{-\gamma_3 x\sin\theta_3} \tag{C.10}$$

In order to extend the formulation to medium 2, we replace A_1 and B_1 with A_2 and B_2, respectively, jk_1 with γ_2, and η_1 with η_{c2}. Also the phase matching condition (C.10) is used. This yields,

$$\mathbf{E}_2 = \mathbf{E}_2^- + \mathbf{E}_2^+ = \hat{y}(A_2 e^{\gamma_2 z\cos\theta_2} + B_2 e^{-\gamma_2 z\cos\theta_2})e^{-jk_1 x\sin\theta_1} \tag{C.11}$$

$$\mathbf{H}_2 = \hat{x}H_{2x} + \hat{z}H_{2z} \tag{C.12}$$

with

$$H_{2x} = \frac{\cos\theta_2}{\eta_2}(A_2 e^{\gamma_2 z\cos\theta_2} - B_2 e^{-\gamma_2 z\cos\theta_2})e^{-jk_1 x\sin\theta_1} \tag{C.13a}$$

$$H_{2z} = \frac{\sin\theta_2}{\eta_2}(A_2 e^{\gamma_2 z\cos\theta_2} + B_2 e^{-\gamma_2 z\cos\theta_2})e^{-jk_1 x\sin\theta_1} \tag{C.13b}$$

Medium 3 include only a wave propagating downward. This yields,

$$\mathbf{E}_3 = \hat{y}(A_3 e^{\gamma_3 z \cos\theta_3}) e^{-jk_1 x \sin\theta_1} \tag{C.14}$$

$$\mathbf{H}_3 = \hat{x} H_{3x} + \hat{z} H_{3z} \tag{C.15}$$

with

$$H_{3x} = \left(\frac{\cos\theta_3}{\eta_3} A_3 e^{\gamma_3 z \cos\theta_3} \right) e^{-jk_1 x \sin\theta_1} \tag{C.16a}$$

$$H_{3z} = \left(\frac{\sin\theta_3}{\eta_3} A_3 e^{\gamma_3 z \cos\theta_3} \right) e^{-jk_1 x \sin\theta_1} \tag{C.16b}$$

Applying the boundary condition, the tangential components of $\mathbf{E}$ and $\mathbf{H}$ must be continuous at $z = 0$. This yields,

$$\mathrm{E}_{1y}|_{z=0} = \mathrm{E}_{2y}|_{z=0} \quad \text{and} \quad \mathrm{H}_{1x}|_{z=0} = \mathrm{H}_{2x}|_{z=0} \tag{C.17}$$

which leads to

$$A_1 + B_1 = A_2 + B_2 \tag{C.18}$$

$$\frac{\cos\theta_1}{\eta_1}(A_1 - B_1) = \frac{\cos\theta_2}{\eta_2}(A_2 - B_2) \tag{C.19}$$

Similarly, we can apply the boundary condition at $z = -d$. This yields,

$$\mathrm{E}_{2y}|_{z=-d} = \mathrm{E}_{3y}|_{z=-d} \quad \text{and} \quad \mathrm{H}_{2x}|_{z=-d} = \mathrm{H}_{3x}|_{z=-d} \tag{C.20}$$

which leads to

$$(A_2 e^{-\gamma_2 d \cos\theta_2} + B_2 e^{\gamma_2 d \cos\theta_2}) = A_3 e^{-\gamma_3 d \cos\theta_3} \tag{C.21}$$

$$\frac{\cos\theta_2}{\eta_2}(A_2 e^{-\gamma_2 d \cos\theta_2} - B_2 e^{\gamma_2 d \cos\theta_2}) = \frac{A_3 \cos\theta_3}{\eta_3} e^{-\gamma_3 d \cos\theta_3} \tag{C.22}$$

Total reflection coefficient R_{total} is defined as

$$R^{\text{total}} = \frac{B_1}{A_1} \tag{C.23}$$

Thus, solutions of (C.18) through (C.22) yields

$$R^{\text{total}} = \frac{R_{12} + R_{23}\, e^{-2\gamma_2 d \cos\theta_2}}{1 + R_{12} R_{23}\, e^{-2\gamma_2 d \cos\theta_2}} \tag{C.24}$$

where R_{12} is the reflection coefficient of half space between medium 1 and medium 2, R_{23} is the reflection coefficient of half space between medium 2 and medium 3, and d is the depth of medium 2.